



Multi-scale dynamics of scalar transfer in Rayleigh–Taylor turbulent mixing

Dongxiao Zhao¹ , Hussein Aluie²  and Gaojin Li¹ 

¹State Key Laboratory of Ocean Engineering, School of Ocean and Civil Engineering, Shanghai Jiao Tong University, Shanghai 200240, PR China

²Department of Mechanical Engineering and Department of Mathematics, University of Rochester, Rochester, NY 14627, USA

Corresponding author: Gaojin Li, gaojinli@sjtu.edu.cn

(Received 6 November 2024; revised 18 February 2025; accepted 18 March 2025)

Miscible Rayleigh–Taylor (RT) turbulence exhibits a wide range of length scales in both the velocity and density fields, leading to complex deformations of isoscalar surfaces and enhanced mixing due to nonlinear interactions among different scales. Through high-resolution numerical simulations and a coarse-graining analysis, we demonstrate that the variance of the heavy fluid concentration, initially maximised by the unstable stratification, progressively cascades from larger to smaller scales, eventually dissipates at the smallest scale. The transfer of scalar variance, Π^Y , primarily governed by the filtered strain rate tensor, is effectively captured by a nonlinear model that links Π^Y to the isoscalar surface stretching. On the other hand, the backscatter of scalar variance transfer, represented by the negative component of Π^Y , is influenced by the filtered vorticity field. Furthermore, we examine the directional anisotropy of scalar transfer in RT turbulence, enhancing the accuracy of the nonlinear model by separating the horizontal mean of the mass fraction from its fluctuating part.

Key words: stratified turbulence, turbulent mixing

1. Introduction

Rayleigh–Taylor (RT) instability arises when a lighter fluid supports a heavier fluid under the influence of gravity or when a lighter fluid accelerates against a heavier one (Rayleigh 1883; Taylor 1950). The acceleration field amplifies small perturbations on the fluid interface, driving the heavy and light fluids to interpenetrate, which eventually results

in the development of turbulent flows. This phenomenon inherently produces a non-stationary, inhomogeneous and anisotropic flow, accompanied by an enhanced mixing process. The RT instability and its associated turbulence play a crucial role in numerous scientific and engineering applications, including supernova explosions (Hillebrandt & Niemeyer 2000; Wang & Chevalier 2001; Zingale *et al.* 2005; Cabot & Cook 2006), the upwelling and overturning of stratified fluids (Tseng & Ferziger 2001; Cui & Street 2004), inertial confinement fusion (Amendt *et al.* 2002; Betti & Hurricane 2016; Zhang *et al.* 2018*a*; Xin *et al.* 2019; Zhang *et al.* 2020; Campbell *et al.* 2021) and combustion (Ashurst 1996; Keenan, Makarov & Molkov 2014; Sykes, Gallagher & Rankin 2021). Due to its significance and inherent complexities, the RT instability has been extensively studied through analytical, experimental and numerical approaches, which have been covered by several extensive reviews in recent years (Abarzhi 2010*b*; Livescu 2013, 2020; Boffetta & Mazzino 2017; Zhou 2017*a,b*; Banerjee 2020; Schilling 2020; Zhou *et al.* 2021*c*; Zhou, Sadler & Hurricane 2025).

1.1. Non-stationary development of RT turbulence

During the early stages of RT instability, different modes composing the small initial perturbation at the interface between the two fluids grow exponentially and independently of each other, until they saturate when the perturbation amplitude becomes comparable to the wavelength of each mode. After this point, nonlinear interactions dominate, leading to the formation of coherent structures such as rising bubbles and sinking spikes. When initial perturbation is composed solely of high wavenumber components (Dimonte *et al.* 2004), RT instability can enter a self-similar regime characterised by a quadratic temporal growth of the mixing width (Ristorcelli & Clark 2004). Further evolution eventually leads to a transition to turbulence (Cook, Cabot & Miller 2004), significantly enhancing both energy transfer and material mixing rates. During the self-similar stage, including the fully turbulent phase, statistics such as growth rate, mixing rate and interfacial surface area follow stable power-law scalings with time, though some weak dependencies on the Reynolds number are observed (Cabot & Cook 2006).

Several phenomenological models have been proposed to explain the temporal behaviour of RT turbulence. Chertkov (2003) proposed a widely used model for three-dimensional (3-D) Boussinesq RT flows with negligible density variation, assuming that the release of potential energy, which primarily occurs at large scales, is slower compared with the energy transfer at intermediate to small scales. This model predicts that the integral length scale, velocity fluctuation in the inertial range and viscous length scale have power-law time dependences, and the forward energy cascade as well as the $-5/3$ scaling of energy spectrum can be established. This theory has been numerically confirmed (Boffetta *et al.* 2009; Matsumoto 2009) and subsequently extended by a Monin–Yaglom relation connecting the third-order structure function with the dissipation rate in RT turbulence (Soulard 2012). Other models, such as those proposed by Zhou (2001); Poujade (2006), and Abarzhi (2010*a*), predict different energy spectra scaling exponents based on different assumptions by incorporating varying levels of complexity of the flow physics. However, the time-dependent statistics is manifested in all these models, emphasising the statistically non-stationary nature of RT turbulence evolution.

There is currently no universal theory applicable to all RT turbulence configurations, due to the intrinsic challenges including its transient, inhomogeneous and variable-density nature. Furthermore, the diverse formulations used to describe RT systems, including the non-equilibrium discrete Boltzmann method (Xu *et al.* 2012; Lai *et al.* 2016; Chen, Xu & Zhang 2018; Zhang *et al.* 2021; Chen *et al.* 2022), the lattice Boltzmann method

(He, Chen & Zhang 1999; Biferale *et al.* 2010; Liang *et al.* 2016), compressible flows (Gauthier & Le Creurer 2010; Gauthier 2017; Zhao, Liu & Lu 2020), incompressible variable-density flows (Cook & Zhou 2002; Livescu & Ristorcelli 2007, 2008) and the Boussinesq approximation (Boffetta *et al.* 2009; Matsumoto 2009; Boffetta & Mazzino 2017), make it difficult to compare corresponding analytical or numerical results. In this paper we adopt a description based on miscible compressible fluids, and previous findings (Zhao *et al.* 2020; Zhou *et al.* 2021*b*; Zhao, Betti & Aluie 2022) indicate the existence of a Kolmogorov forward cascade for kinetic energy (KE) in such systems. We should note that when studying hydrodynamic instabilities involving very small scales or rarefied gases, such as interstellar plasmas, molecular fluctuations can be significant (Xu *et al.* 2016; Buttler, Williams & Najjar 2017; Liu *et al.* 2023; Zhang *et al.* 2023; Majumder, Livescu & Girimaji 2024). In these cases, the discrete Boltzmann method is more suitable for analysing the mixing process (Xu, Zhang & Gan 2024).

1.2. Multi-scale mixing statistics in RT turbulence

Initially, the concentration field in RT turbulence begins with pure heavy and light fluids segregated. Once the instability develops, the multi-scale velocity field distorts and stretches the interface between the fluids, increasing its surface area and enhancing molecular mixing at small scales. Consequently, mixing in RT turbulence emerges as a multi-scale process, driven by both small-scale mass diffusion and large-scale entrainment caused by the stirring effects of the velocity field (Villermaux 2019).

Although the scalar or concentration field is transported by the fluid velocity, its multi-scale dynamics can differ significantly from those of the velocity field. For instance, the intermittency level of a passive scalar is generally found to be higher than that of the velocity field (Warhaft 2000), and even a random Gaussian background velocity can induce non-Gaussian intermittency of the passive scalar field. Therefore, it is crucial to determine the multi-scale dynamics of the concentration field in RT turbulence and its connection with the velocity and the velocity gradient. An appropriate metric for quantifying the effects of multi-scale mixing should account for both large-scale entrainment and small-scale diffusion processes.

Previous research on RT mixing has primarily focused on single-point statistics, such as mixing width and the mixedness parameter. However, these averaged measures primarily reflect small-scale molecular mixing and do not adequately account for large-scale entrainment processes that can significantly enhance molecular mixing. For instance, the mixedness parameter is defined as $\Theta = \int_{-\infty}^{\infty} \langle X(1-X) \rangle_{xy} dz / \int_{-\infty}^{\infty} \langle X \rangle_{xy} \langle 1-X \rangle_{xy} dz$, where X represents the mole fraction of the heavy or light fluid and $\langle \cdot \rangle_{xy}$ denotes an average over the horizontal plane. If only diffusion is active, with no convection, this parameter would equal 1 within a fully mixed region. Conversely, if only large-scale entrainment occurs without diffusion, the mole fraction field remains a rearrangement of pure fluids (only 0 or 1), resulting in Θ being zero. Therefore, in the context of miscible RT turbulence, where the entrainment process is the initial step toward enhanced diffusion and molecular mixing, the mixedness parameter Θ is inadequate for quantifying this multi-scale mixing process. Similarly, the probability density function (PDF) of the concentration and its associated moments (mean and variance) are also insufficient metrics, as the PDF remains unaffected by large-scale entrainment alone.

Two-point statistics, which measures the inter-scale transfer of concentration, are more suitable for describing the multi-scale characteristics of mixing processes. For instance, inter-scale scalar transfer was studied by Yaglom *et al.* (1949), leading to the well-known 4/3 law for the structure function of passive scalars in homogeneous turbulence:

$\langle \delta u_L(\mathbf{x}; r) \delta \theta(\mathbf{x}; r)^2 \rangle = -4/3 \epsilon_\theta r$, where $\delta u_L(r)$, $\delta \theta(r)$ are the longitudinal velocity increment and scalar increment across the separation length r , ϵ_θ is the mean dissipation rate of scalar energy and $\langle \cdot \rangle$ represents spatial averaging. This result was later verified and extended to boundary layer flows (Danaila *et al.* 1997), turbulence at low Schmidt numbers (Iyer & Yeung 2014) and grid-generated turbulence (Meyer, Mydlarski & Danaila 2018). Recently, Wang *et al.* (2023) studied the nonlinear scalar transfer in grid-generated passive scalar turbulence with a mean scalar gradient perpendicular to the flow direction, using a Kármán–Howarth–Monin–Hill equation for the scalar increment. They found an inverse scalar energy transfer from small to large scales in the upstream region, driven by negative transfer along the scalar gradient direction, while in the downstream region, the transfer occurs from large to small scales. However, when the flow is driven parallel to the scalar gradient such as in RT flows, the mechanism of scalar transfer across different scales remains unclear. To the best of the authors’ knowledge, quantitative measurements of inter-scale scalar transfer, including point-split or filtering analyses of the concentration field budget, have not yet been considered for RT turbulence.

By adopting the approach of scale decomposition and coarse graining, we can treat the diffusion process and large-scale entrainment on equal footing at coarse-grained levels. In this context, turbulent eddy diffusivity, which drives large-scale entrainment, plays a role analogous to molecular diffusivity at small scales. Several existing measures of mixing efficiency treat the reversible stirring and irreversible mixing equivalently, such as the coarse-grained density and segregation metrics in Krasnopolskaya *et al.* (1999), and mixed norms or negative Sobolev norms in Mathew, Mezić & Petzold (2005). However, these metrics are not directly connected to the underlying flow dynamics. In this paper we aim to describe the multi-scale mixing dynamics of RT turbulence directly through coarse-grained budget equations of the concentration field.

1.3. Anisotropy in RT turbulence

Anisotropy at various length scales is a key characteristic of RT turbulence. Due to the effects of external acceleration and the initial unstable stratification, the properties of RT turbulence in the vertical direction can differ significantly from those in the horizontal directions. Several metrics are used to quantify anisotropy in turbulent flows, the most common being vector component anisotropy, variance anisotropy and spectral anisotropy (Oughton *et al.* 2016). Vector component anisotropy refers to the unequal distribution among the three components of a vector field, while variance anisotropy is defined by the inequality among the diagonal elements of the variance tensor $\langle u_i u_j \rangle - \langle u_i \rangle \langle u_j \rangle$ for a vector field u_i . Both of these metrics describe directional anisotropy. In contrast, spectral anisotropy captures variations in spectral energy distribution when the components of the associated wavevector are varied independently (Shebalin, Matthaeus & Montgomery 1983; Oughton *et al.* 2016; Zhao & Aluie 2023). This concept primarily quantifies differences in characteristic length scales associated with each spatial direction and can be seen as a form of shape anisotropy of the eddies related to any field variable. In this work we shall focus on the directional anisotropy at different length scales during RT evolution.

In RT turbulence, vector component anisotropy has been studied by Cabot & Zhou (2013), who measured the differences between the components of various vector and tensor fields, including horizontally averaged velocity, vorticity and velocity derivatives. Their findings revealed that vertical velocity is significantly higher than horizontal velocity, while the behaviour of velocity derivatives differs between transverse and longitudinal components. Additionally, Cabot & Zhou (2013) analysed the one-dimensional longitudinal and transverse spectra for velocity and vorticity components,

showing that while isotropy is observed at small scales, anisotropy becomes apparent at larger scales.

Similarly, variance anisotropy in RT turbulence can be quantified using the Reynolds stress anisotropic tensor, $b_{ij} = \langle u_i u_j \rangle / \langle |\mathbf{u}|^2 \rangle - (1/3)\delta_{ij}$. A typical value of $b_{zz} = 0.3$ across the mixing layer is observed (Ristorcelli & Clark 2004; Livescu *et al.* 2009), indicating a dominance of vertical turbulent KE as a result of the vertical gravity injection. This measure has also been applied in Fourier space (Livescu *et al.* 2009; Gauthier 2017), where $b_{zz}(k)$ approaches zero at intermediate scales, suggesting isotropy, while anisotropy persists at both large and small scales due to the influence of buoyancy forcing. Most previous studies on RT turbulence have focused on the anisotropy of the velocity field, whereas research on the scalar field is relatively limited, primarily focusing on the anisotropy of length scales or spectra associated with the scalar field (Gauthier 2017; Zhou & Cabot 2019).

Understanding the directional anisotropy of RT turbulence is essential for developing numerical models used in large-eddy simulations (LES) or Reynolds-averaged Navier–Stokes (RANS) simulations for inhomogeneous and anisotropic turbulence. Traditional LES models such as the Smagorinsky model (Smagorinsky 1963) or the nonlinear model (Clark, Ferziger & Reynolds 1979), designed for isotropic turbulence, perform reasonably well in RT turbulence (Zhou *et al.* 2021a; Luo *et al.* 2023) in terms of overall statistics. In the following sections we show that while a nonlinear model accurately captures the overall statistics of the scalar budget, it fails to predict the directional anisotropic behaviour. However, focusing exclusively on the fluctuating component of the scalar field (subtracting the horizontally averaged vertical profile) leads to improved predictions of anisotropy. This finding indicates that, in modelling RT turbulence, it is crucial to treat the horizontally averaged and fluctuating components separately.

The subsequent sections are organised as follows. Section 2 presents the governing equations and details of the numerical simulations. In § 3 we provide simulation results and the temporal evolution of RT mixing statistics. Section 4 delves into the scale transfer of the concentration field, examining its relationship with the strain rate and vorticity fields. In § 5 we analyse the directional anisotropy of KE and concentration, focusing particularly on the anisotropic behaviour of scalar variance transfer. Finally, § 6 summarises the physical mechanisms driving the multi-scale mixing process in RT turbulence and concludes the discussion.

2. Governing equations and numerical methods

We adopt the compressible miscible Navier–Stokes equations with two fluid species to describe the RT turbulent flow, including the conservation of mass, mass fraction, momentum and total energy (Gauthier 2017; Zhao *et al.* 2023):

$$\frac{\partial \rho}{\partial t} + \nabla \cdot (\rho \mathbf{u}) = 0, \quad (2.1)$$

$$\frac{\partial \rho Y_k}{\partial t} + \nabla \cdot (\rho \mathbf{u} Y_k) = \nabla \cdot (\rho D \nabla Y_k), \quad (2.2)$$

$$\frac{\partial \rho \mathbf{u}}{\partial t} + \nabla \cdot (\rho \mathbf{u} \mathbf{u}) = -\nabla P + \nabla \cdot \boldsymbol{\sigma} + \rho \mathbf{g}, \quad (2.3)$$

$$\frac{\partial \rho E}{\partial t} + \nabla \cdot ((\rho E + P)\mathbf{u}) = \nabla \cdot (\boldsymbol{\sigma} \cdot \mathbf{u}) + \rho \mathbf{u} \cdot \mathbf{g} - \nabla \cdot \mathbf{q}. \quad (2.4)$$

Here ρ , \mathbf{u} , P are the density, velocity and pressure fields, respectively, $\mathbf{g} = (0, 0, -g)$ is the gravitational acceleration along the negative vertical direction, Y_k is the mass fraction of the k th component, $k = h$ and l for heavy and light fluids respectively, and $E = (1/2)u^2 + c_v T$ is the total energy density, in which c_v is the specific heat at constant volume and T is temperature. $\mathbf{q} = -\kappa \nabla T$ is the heat flux vector, $\boldsymbol{\sigma} = 2\mu(\mathbf{S} - (1/3)\text{tr}(\mathbf{S})\mathbf{I})$ is the viscous stress tensor, $\mathbf{S} = (\nabla \mathbf{u} + \nabla \mathbf{u}^T)/2$ is the strain rate tensor, \mathbf{I} is the identity tensor and μ , D , κ are the dynamic viscosity, mass diffusivity and thermal conductivity, respectively.

The above set of equations is complemented by the ideal gas equation of state, $P = \rho \tilde{R} T (Y_h/W_h + Y_l/W_l)$, where \tilde{R} is the universal gas constant, W_h , W_l are the molecular weights of the two species. By setting equal molecular weights $W_h = W_l = W$, the ideal gas equation of state reduces to $P = \rho(\tilde{R}/W)T$, and the mass fraction equation (2.2) is thus decoupled from other equations and acts as a passive scalar. Additionally, due to the constraint $Y_h + Y_l = 1$, only one of the mass fraction equations (2.2) is required to solve the system. Henceforth, unless otherwise stated, we use Y to denote the mass fraction of the heavy fluid.

The computational domain is a rectangular box with dimensions of $L_x \times L_y \times L_z = 0.8 \times 0.8 \times 1.6$, containing an isopycnal initial density profile. In this set-up, the upper half of the domain is filled with a uniform heavy fluid of density ρ_h and the lower half with a light fluid of density ρ_l . Consequently, the mass fraction of the heavy fluid is $Y = 1$ in the upper half and $Y = 0$ in the lower half, with the corresponding Atwood number given by $At = (\rho_h - \rho_l)/(\rho_h + \rho_l)$. The initial pressure field satisfies the hydrostatic condition $\partial P/\partial z = -\rho g$ and the initial temperature is derived from the ideal gas equation of state. An initial perturbation is applied to the vertical velocity field near the interface between the heavy and light fluids, with energy distributed equally across the wavenumber shells $k \in [32, 64]$, corresponding to the bubble merger regime in RT turbulence. Boundary conditions are periodic in the horizontal directions, with no-slip walls at the top and bottom boundaries. The temperature and mass fraction fields have zero-gradient boundary conditions at the top and bottom walls. The system of equations (2.1)–(2.4) is solved numerically using a pseudo-spectral method in the horizontal direction and a sixth-order compact finite difference scheme in the vertical direction. To prevent contamination from high wavenumbers due to nonlinearity, the 2/3 dealiasing rule (Patterson & Orszag 1971) and a compact filtering scheme (Lele 1992; Brady & Livescu 2019) are applied. Further details can be found in Zhao *et al.* (2022).

In the subsequent sections we adopt the coarse-graining approach to decompose turbulence fields into different scales. Coarse graining applied to any 3-D field $f(\mathbf{x})$ is a low-pass filtering defined by a convolution

$$\bar{f}_\ell(\mathbf{x}) = \int d^3\mathbf{r} G_\ell(\mathbf{r}) f(\mathbf{x} - \mathbf{r}), \tag{2.5}$$

where the normalised kernel $G_\ell(\mathbf{r}) = \ell^{-3} G(\mathbf{r}/\ell)$ is a dilated kernel with a characteristic width ℓ . The coarse graining defined in (2.5) decomposes the field $f(\mathbf{x})$ into a large-scale ($\gtrsim \ell$) component \bar{f}_ℓ and a small-scale ($\lesssim \ell$) component $f'_\ell = f - \bar{f}_\ell$. This approach is widely adopted in LES to separate the resolved-scale and subgrid-scale dynamics (Meneveau & Katz 2000a), and the Gaussian filter, due to its positivity in both physical and Fourier spaces, is commonly adopted as the filtering kernel. Since the Gaussian filter is separable, for isotropic filtering in Cartesian coordinates, we adopt

$$G_\ell(x, y, z) = \left(\sqrt{\frac{6}{\pi \ell^2}} \right)^3 \exp \left(-\frac{6}{\ell^2} (x^2 + y^2 + z^2) \right), \tag{2.6}$$

Label	Grid size	L_x	L_y	L_z	μ	At	Gr	Re	Re_h	$\eta/\Delta x$
Low-At	$512 \times 512 \times 1024$	0.8	0.8	1.6	1×10^{-5}	0.15	8.63	6974	11044	0.64
Mid-At	$512 \times 512 \times 1024$	0.8	0.8	1.6	1×10^{-5}	0.5	16.95	9398	16164	0.51
High-At	$256 \times 256 \times 512$	0.8	0.8	1.6	4×10^{-5}	0.8	9.42	3276	5971	0.84
Low-iLES	$512 \times 512 \times 1024$	0.8	0.8	1.6	1.15×10^{-6}	0.15	472	85049	171016	0.10

Table 1. Parameters of the RT simulations conducted in this study. The domain lengths in the three directions are denoted by L_x , L_y and L_z , and At represents the Atwood number. Gravitational acceleration is set to $g = 1$ in the $-z$ direction. The mesh Grashof number is defined as $Gr = 2At g \langle \rho \rangle^2 \Delta x^3 / \mu^2$, the Kolmogorov scale as $\eta = \mu^{3/4} / (\epsilon^{1/4} \langle \rho \rangle^{3/4})$ and the Reynolds number as $Re = \langle |u|^2 \rangle^{1/2} L_x \langle \rho \rangle / \mu$, where $\langle \cdot \rangle$ denotes the spatial mean over the whole simulation domain and ϵ is the KE dissipation rate. The outer-scale Reynolds number is defined as $Re_h = \langle \rho \rangle h \bar{h} / \mu$, where $h(t)$ is the mixing width defined in (3.1). The mass diffusivity D is set to be equal to the dynamic viscosity μ . In the table, the Reynolds number and Kolmogorov scale are calculated at the dimensionless time $\hat{t} = t / \sqrt{(L_x / At) g} = 5.0$.

where the filtering width is the same along the three Cartesian coordinates.

In complex flows such as RT turbulence, special treatment is needed for coarse graining near walls. We extend the domain beyond the physical boundaries with values consistent with the boundary conditions. For RT flows, the velocity is set to zero beyond the walls, the density and mass fraction fields are held constant due to zero-gradient conditions, while the extended pressure field satisfies the hydrostatic condition $dP/dz = -\rho g$ (Zhao & Aluie 2018; Zhao *et al.* 2022). This approach enables filtering throughout the domain without resorting to inhomogeneous filtering near the wall.

3. Temporal evolution of mixing statistics

We perform numerical simulations of RT turbulence at low- to high-Atwood numbers, with $At = (\rho_h - \rho_l) / (\rho_h + \rho_l) = 0.15, 0.5$ and 0.8 , respectively. The parameters are shown in table 1. All simulations have a spatially uniform dynamic viscosity μ and unity Prandtl number $Pr = c_p \mu / \kappa = 1$, with κ the thermal conductivity and $c_p = 2$ the specific heat capacity at constant pressure. The grid size is checked to satisfy the criterion for adequate resolution of the smallest scales, $k_{\max} \eta \geq 1.5$ (Yeung & Pope 1989), where k_{\max} is the maximum resolved wavenumber and $\eta = \mu^{3/4} / (\epsilon^{1/4} \langle \rho \rangle^{3/4})$ is the Kolmogorov scale. The temporal evolution of the Kolmogorov scale η is shown in figure 16 in Appendix A, indicating an adequate resolution during the time span studied in this paper. In the following sections we primarily focus on the low- and mid-At cases. However, for completeness and verification purposes, we have also added two additional simulations: one labelled high-At for a simulation at $At = 0.8$ and another labelled low-iLES for an implicit LES performed at $At = 0.15$. The implicit LES simulation, which solves the same set of equations (2.1)–(2.4) on an under-resolved grid, satisfies the mixing transition criterion for RT turbulence (Zhou, Robey & Buckingham 2003; Qi *et al.* 2024; Xiao, Qi & Zhang 2025; Xie *et al.* 2025) for outer-scale Reynolds numbers greater than 1.6×10^5 . In Appendix E we verify that the main results for the low- and mid-At cases are also applicable to the high-At and low-iLES cases.

3.1. Evolution of the mixing layer

Figure 1 shows the visualisations of the mass fraction fields Y for the low-At and mid-At cases at dimensionless time $\hat{t} = t \sqrt{Atg/L_x} = 4.5$, where $\sqrt{L_x/(Atg)}$ is the characteristic time scale of RT flows. The flow encompasses a wide range of length scales, and the

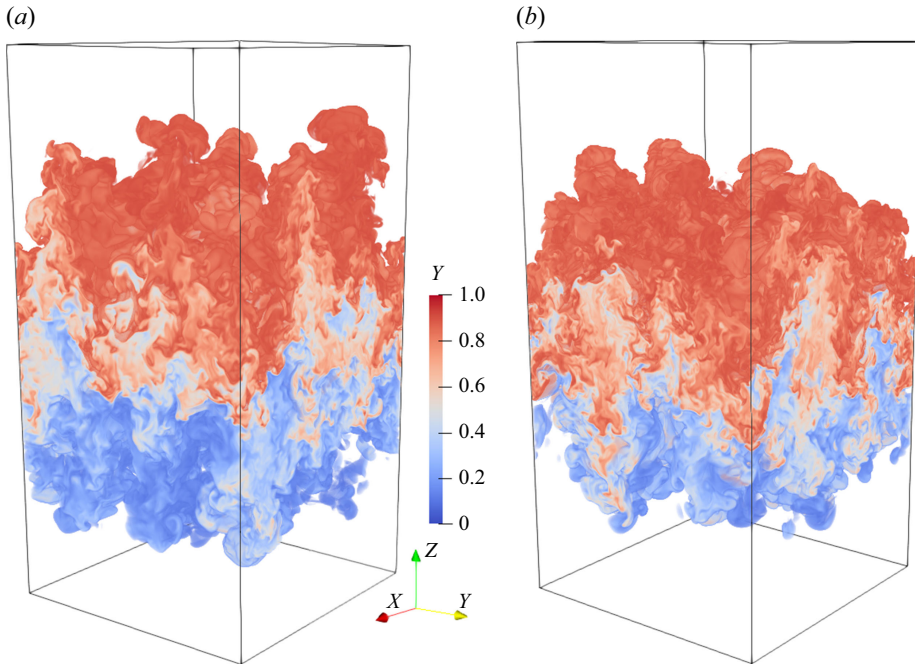


Figure 1. Visualisations of the mass fraction fields Y at dimensionless time $\hat{t} = t\sqrt{Atg/L_x} = 4.5$ for (a) low-At case at $At = 0.15$, and (b) mid-At case at $At = 0.5$.

mixing zone heights are similar for the two cases. A quantitative measure of the mixing zone growth is the mixing width $h(t)$, defined as (Cabot & Cook 2006; Zhang *et al.* 2018b)

$$h(t) = \frac{2}{\rho_h - \rho_l} \int_{-\infty}^{\infty} \min(\langle \rho \rangle_{xy} - \rho_l, \rho_h - \langle \rho \rangle_{xy}) dz, \quad (3.1)$$

where $\langle \cdot \rangle_{xy} = (1/L_x L_y) \iint (\cdot) dx dy$ is a horizontally averaged quantity (a function of z) and ρ_l, ρ_h are densities of the light and heavy fluids. In figure 2(a) the mixing width exhibits quadratic growth with time for both cases after $\hat{t} > 2$, suggesting a self-similar expansion of the RT mixing zone. The fitted growth rate coefficient α , appearing in the quadratic growth expression $h(t) = \alpha At gt^2$, is 0.0232 for the low-At case and 0.0209 for the mid-At case, both of which fall within the range reported in the literature (Zhou 2017a).

A related metric is the mixedness parameter, Θ (see introduction), which measures the degree of molecular mixing along horizontal planes and is defined as

$$\Theta = \frac{\int_{-\infty}^{\infty} \langle Y(1 - Y) \rangle_{xy} dz}{\int_{-\infty}^{\infty} \langle Y \rangle_{xy} \langle 1 - Y \rangle_{xy} dz}. \quad (3.2)$$

The parameter Θ is intended to measure the rate of reaction in a mixture, in which the molar fraction shall be adopted in the above definition instead of mass fraction (Youngs 1991; Wilson & Andrews 2002). Here in our RT configuration, the molecular weights of the two fluids are assumed to be equal, so the mass fraction is equal to the molar fraction, making the use of the above definition appropriate.

Figure 2(b) shows that initially, the presence of a small transition region near the fluid interface results in well-mixed flow within this region, leading to $\Theta \approx 1$. The parameter stays around 1 for $\hat{t} < 1$ during which the diffusion effect is dominant and the instability

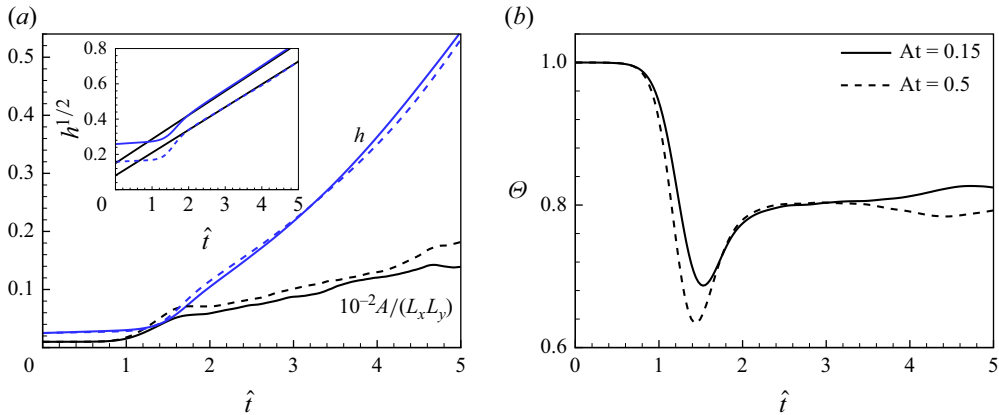


Figure 2. Evolution of (a) the total mixing width h and the area $A/(L_xL_y)$, and (b) the mixedness parameter Θ of the isosurface $Y = 0.5$ for the low- At and mid- At simulation cases. In the inset of panel (a), the square root of the mixing width is depicted to measure the growth coefficient α corresponding to the quadratic growth rate $h(t) = \alpha Atg^2$ marked by the black solid lines. The low- At case in the inset is shifted upward by 0.1 to distinguish it from the mid- At case, and the corresponding α values are 0.0232 and 0.0209 for the low- At and mid- At cases, respectively. Throughout this work, solid and dashed lines represent the low- At and mid- At cases, respectively, unless otherwise specified.

has yet to grow. After this transient period, the instability grows and the fluid is dominated by advection. The fluid interface stretches and folds, causing large regions of unmixed pure fluids to be entrained into the mixing zone, which reduces the mixedness parameter Θ . As the entrainment process progresses, the interfacial area increases, enhancing diffusion at these interfaces, which is reflected by a subsequent rise in Θ between $1.5 \leq \hat{t} \leq 2$. After $\hat{t} > 2$, the effect of advection and entrainment of pure fluids (which decreases Θ) balances with the effect of interface diffusion (which increases Θ), leading to a saturation of Θ around 0.8, consistent with results in Cook *et al.* (2004); Banerjee & Andrews (2009).

To further reveal the roles of advection and diffusion, in figure 2(a) we also show the evolution of the normalised area $A/(L_xL_y)$ of the $Y = 0.5$ isosurface, obtained using the marching cube algorithm (Lorenson & Cline 1998). The algorithm divides space into voxels (small cubes), interpolates isosurface intersections along their edges and connects these points based on vertex positions to form a piecewise-linear isosurface approximation. In accordance with the evolution of the mixedness Θ , the isosurface areas are close to flat with a value of L_xL_y during $\hat{t} < 1$, while they increase rapidly within $1 < \hat{t} < 1.5$ and the growths are close to exponential, similar to the area increase of a material surface in isotropic turbulence (Batchelor 1952). After $\hat{t} > 1.5$, the enhanced diffusional effect hinders the growth of the isosurface area, and the exponential growth rate shifts towards a nearly linear growth in time after $\hat{t} > 2$, during which the system is self-similar and the mixedness parameter remains roughly constant.

Unlike the mixing width, the interfacial area of the mid- At case is consistently larger than that of the low- At case, suggesting that the isosurface is more wrinkled with a greater heavy–light density contrast, and therefore, more potential energy is injected into the system. A quantitative measure of these interfacial topologies, shown in figure 3(a) for isosurfaces or figure 3(c) for cross-sectional isolines, is the fractal dimension, D_3 and D_2 , embedded in 3-D and two-dimensional (2-D) space, respectively. The fractal dimension is calculated using the box-counting algorithm (Mandelbrot 1982; Sreenivasan & Meneveau

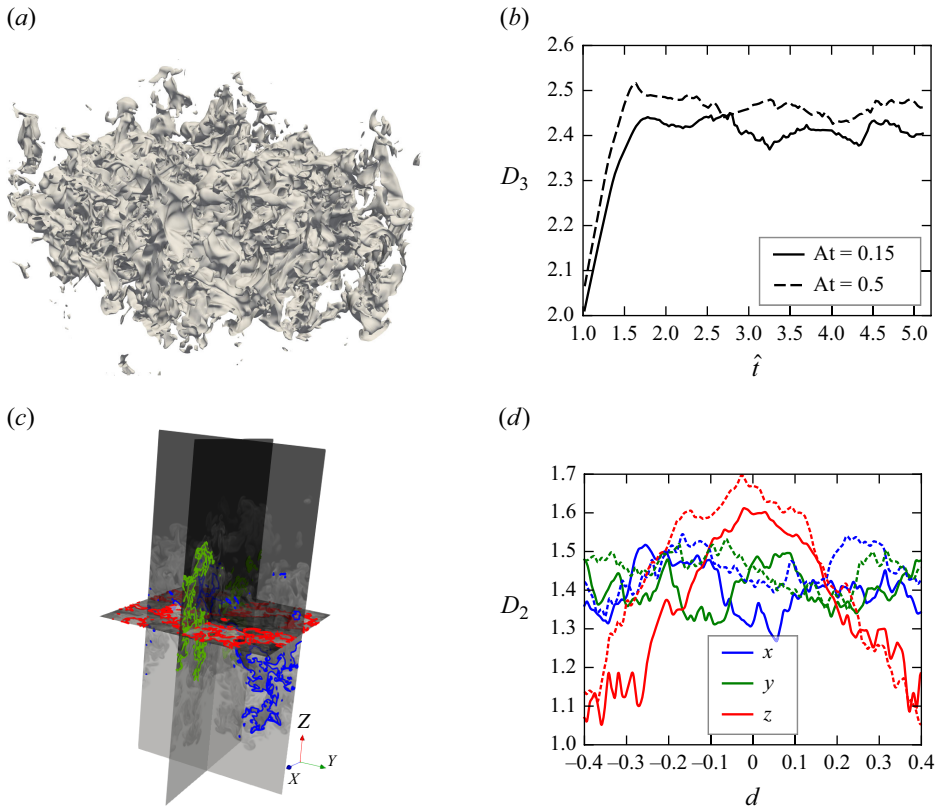


Figure 3. (a) Visualisation of the isosurface of the low- At case at $\hat{t} = 5$. (b) The temporal evolution of the fractal dimension D_3 of the isosurfaces, measured with the box-counting algorithm (Mandelbrot 1982). (c) Visualisation of isolines on three 2-D slices along the x -, y -, and z -normal directions for the low- At case at $\hat{t} = 5$. (d) The fractal dimension D_2 of the isolines at different slice locations d , where d denotes the x , y , or z location of the slices relative to the domain centre. The low- At cases are shown in solid lines, while the mid- At cases are in dashed lines.

1986), as detailed in Appendix B. Here, $D_3 = 1 + D_2$ (Sreenivasan & Meneveau 1986), and a larger fractal dimension indicates a more complex interfacial manifold.

Temporal evolution of the fractal dimension is depicted in figure 3(b), which tracks the evolution of D_3 for the $Y = 0.5$ isosurfaces. Between $1 \leq \hat{t} \leq 1.5$, the isoscalar surfaces rapidly evolve from a flat surface with a dimension of 2.0 to a highly distorted level set. After this transient phase, in the self-similar regime for $\hat{t} > 2$, the fractal dimension stabilises around 2.41 for the low- At case and 2.46 for the mid- At case. Compared with reported values of $D_2 = 1.7\text{--}1.8$ for 2-D RT turbulence (Hasegawa, Nishihara & Sakagami 1996) and $D_2 \leq 1.3$ for 3-D RT turbulence (Linden, Redondo & Youngs 1994), both obtained from simulations without viscosity or mass diffusion, the RT isosurfaces in our 3-D simulations display different fractal behaviour when diffusion effects are included. Furthermore, the anisotropy in RT turbulence is manifested in the fractal dimension of isolines on different cross-sections. In figure 3(d) the fractal dimension of the $Y = 0.5$ isolines on cross-sections in the x -, y -, and z -normal planes is shown for both low- At and mid- At cases at $\hat{t} = 5$. The variable d represents the location of the embedded plane relative to the domain centre. In both cases, isolines on x - and y -normal planes exhibit similar fractal dimensions, with mean values of 1.4 for the low- At case and 1.45 for the

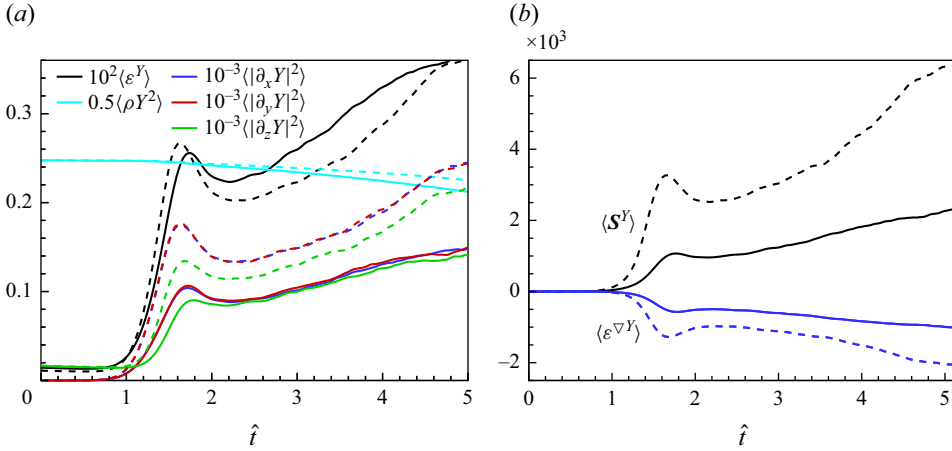


Figure 4. (a) Temporal evolution of the the mean scalar dissipation $\langle \varepsilon^Y \rangle$, the mean scalar energy $\langle (1/2)\rho Y^2 \rangle$, as well as the three components of the mean squared mass fraction gradient. (b) The evolution of the mean scalar element stretching $\langle S^Y \rangle$ and the mean scalar gradient dissipation $\langle \varepsilon^{\nabla Y} \rangle$. Solid and dashed lines represent the low-At and mid-At cases, respectively.

mid-At case. In comparison, isolines on the z -normal planes exhibit a fractal dimension of approximately 1 at the edges of the mixing zone (large d magnitude), while in the middle region ($d \approx 0$), the peaks of D_2 exceed the values of the x - and y -normal isolines. This anisotropic behaviour of D_2 reflects the anisotropic transport of the scalar field.

3.2. Evolution of scalar variance and gradient magnitude

In RT turbulence the evolution of the scalar field variation is crucial in determining the mixing dynamics. Similar to the equations for turbulent KE and strain/vorticity dynamics, we analyse the governing equations for scalar field variance and its gradient, which are

$$\rho \frac{D}{Dt} \frac{1}{2} Y'^2 = - \underbrace{\rho D |\nabla Y'|^2}_{\varepsilon^Y} + \nabla \cdot \left(\rho D \nabla \frac{Y'^2}{2} \right), \quad (3.3)$$

$$\frac{D}{Dt} \frac{1}{2} |\nabla Y|^2 = \underbrace{-\nabla Y \cdot \mathbf{S} \cdot \nabla Y}_{S^Y} + \underbrace{\nabla Y \cdot \nabla \left[\frac{1}{\rho} \nabla \cdot (\rho D \nabla Y) \right]}_{\varepsilon^{\nabla Y}}, \quad (3.4)$$

where D/Dt is the material derivative, $Y' = Y - Y_0$ is the fluctuating part of mass fraction and $Y_0 = \langle \rho Y \rangle / \langle \rho \rangle$ is the density-weighted mean concentration. Note that the equation for Y^2 has the same expression as (3.3) for Y'^2 , since Y_0 remains constant over time due to the conservations of both mass and mass fraction. Here, we define new terms ε^Y , S^Y and $\varepsilon^{\nabla Y}$, which denote the scalar dissipation rate, the scalar element stretching rate and the scalar gradient dissipation rate, respectively.

Equation (3.3) indicates that the spatial mean concentration variance, when scaled by density, decreases monotonically over time, with a decreasing rate of $\langle \varepsilon^Y \rangle$. In figure 4(a) we present the temporal evolution of the mean mass fraction energy, $\langle (1/2)\rho Y^2 \rangle \equiv \langle (1/2)\rho Y'^2 \rangle + (1/2)\langle \rho \rangle Y_0^2$, instead of the variance $\langle (1/2)\rho Y'^2 \rangle$, to have the same initial value between the low-At and mid-At cases. The results confirm the monotonic decay of concentration energy, and consequently, the mass fraction variance. Initially, the concentration energy is slightly less than 0.25, corresponding to fully segregated heavy

and light fluids ($Y = 1, \rho_h = 1$ on the upper half-domain so that $\langle (1/2)\rho Y^2 \rangle|_{t=0} = 0.25$), except in a narrow region near the fluid interface. The decay rate is slow for $\hat{t} < 1.5$, before the onset of turbulence, but after $\hat{t} > 2$, during the self-similar phase, the decay rates for both cases increase, accompanied by a growing scalar gradient magnitude $\langle |\nabla Y|^2 \rangle$. Notably, the decay rate in the low-At case is faster than in the mid-At case, despite the reverse trend in the relative magnitude of the scalar gradient. This trend indicates that the density difference of the light fluids between the two cases outweighs the differences in scalar gradient magnitudes, and the constant mass diffusivity adopted in the simulations leads to a higher scalar dissipation rate ε^Y for the low-At case.

The scalar gradient magnitude budget equation (3.4) indicates that $(1/2)|\nabla Y|^2$ is not a conserved invariant due to surface stretching, unlike the scalar field itself. The second term on the right-hand side, $\varepsilon^{\nabla Y}$, represents the dissipation of the scalar gradient, with its mean value being consistently negative and approximately equal to $\langle -D(\nabla^2 Y)^2 \rangle$ in the $At \rightarrow 0$ limit. The blue lines in figure 4(b) confirm that the spatial mean value of $\varepsilon^{\nabla Y}$ is always negative. In contrast, the first term S^Y on the right-hand side is a primary source term in the growth of $(1/2)|\nabla Y|^2$ for RT flows. To confirm that S^Y indeed represents the stretching of scalar elements, we express it as

$$S^Y = -\nabla Y \nabla Y : \mathbf{S} = -|\nabla Y|^2 \mathbf{nn} : \nabla \mathbf{u} \approx |\nabla Y|^2 (\mathbf{I} - \mathbf{nn}) : \nabla \mathbf{u}, \quad (3.5)$$

where $\mathbf{n} = \nabla Y / |\nabla Y|$ is the normal vector of the mass fraction isosurface pointing from the light fluid towards the heavy fluid. The incompressibility condition $\nabla \cdot \mathbf{u} = 0$ approximately holds in the current compressible RT simulations, given that the initial conditions are isopycnal and the Mach numbers are low (Zhao *et al.* 2022). The fractional rate of change of a surface element A is given by $(1/A)(DA/Dt) \equiv (\mathbf{I} - \mathbf{nn}) : \nabla \mathbf{u}$ when surface propagation due to diffusion is negligible (Poinsot & Veynante 2005). Therefore, the right-hand side of (3.5) represents the stretching rate of the mass fraction isosurface along the tangential plane, confirming that S^Y is a weighted stretching term.

Due to the initial stratification, the vertical scalar gradient is greater than the horizontal terms at early times, as is indicated in figure 4(a). However, when $\hat{t} > 1$, the horizontal derivatives of the mass fraction exceed the vertical component, consistent with the formation of coherent bubbles and spikes that are primarily elongated in the vertical direction. Between $1 < \hat{t} < 2$, all components of the scalar gradient undergo a rapid increase followed by a decrease. This behaviour results from the competing effects of advection-induced surface stretching and diffusion-induced scalar gradient dissipation, as described by the right-hand side of (3.4), and corresponds with the non-monotonic evolution of the mixedness parameter Θ during this period, as seen in figure 2(b). After $\hat{t} > 2$, the mean values of the mass fraction gradients increase over time, with directional anisotropy between horizontal and vertical components persisting, especially in the mid-At case with greater density contrast. These results indicate that the horizontal scalar gradient is larger than the vertical one, implying a smaller horizontal gradient length scale, $L_{\Delta,x}$, compared with the vertical length scale, $L_{\Delta,z}$:

$$\frac{1}{L_{\Delta,x}} \equiv \left(\frac{\langle |\partial_x Y|^2 \rangle}{\langle Y^2 \rangle} \right)^{1/2} \geq \frac{1}{L_{\Delta,z}} \equiv \left(\frac{\langle |\partial_z Y|^2 \rangle}{\langle Y^2 \rangle} \right)^{1/2}. \quad (3.6)$$

Physically, this means that at intermediate to small scales (associated with the ∇ operator), the ‘eddies’ formed by the mass fraction field are elongated in the vertical direction relative to the horizontal direction (Zhao & Aluie 2023).

The budget equations for scalar variance (3.3) and scalar gradient (3.4) respectively describe, at large and small scales, the annihilation and creation of the spatial variation

of the transported scalar, suggesting an intrinsic connection between scalar dissipation, ε^Y , and scalar element stretching, S^Y . The time evolution of their spatial mean values shown in figures 4(a) and 4(b) supports this speculation, while the joint PDFs of the two quantities further validate their pointwise correlation (see figure 18 in Appendix C). The results suggest a shared underlying physical mechanism between ε^Y and S^Y , which is analogous to the connection between the pseudo-dissipation rate of KE, $\varepsilon = \nu|\boldsymbol{\omega}|^2$, and the vortex stretching, $\boldsymbol{\omega} \cdot \mathbf{S} \cdot \boldsymbol{\omega}$, where $\mathbf{S} = (1/2)(\nabla\mathbf{u} + \nabla\mathbf{u}^T)$ and $\boldsymbol{\omega} = \nabla \times \mathbf{u}$ are the strain rate tensor and vorticity. Vortex stretching increases local vorticity by stretching vortex tubes, leading to a higher energy dissipation rate. Similarly, in the case of mass fraction, scalar element stretching S^Y amplifies the local scalar gradient, thereby increasing the scalar dissipation rate ε^Y .

To further elucidate the connection between S^Y and ε^Y , we diagonalise the strain rate tensor via eigendecomposition, yielding $\mathbf{S} = \lambda_\alpha \mathbf{e}_\alpha \mathbf{e}_\alpha + \lambda_\beta \mathbf{e}_\beta \mathbf{e}_\beta + \lambda_\gamma \mathbf{e}_\gamma \mathbf{e}_\gamma$, where $\lambda_\alpha \geq \lambda_\beta \geq \lambda_\gamma$ are the eigenvalues and $\mathbf{e}_\alpha, \mathbf{e}_\beta, \mathbf{e}_\gamma$ are the corresponding eigenvectors. This decomposition allows us to express the scalar element stretching as

$$\begin{aligned} S^Y &= -\lambda_\alpha |\nabla Y \cdot \mathbf{e}_\alpha|^2 - \lambda_\beta |\nabla Y \cdot \mathbf{e}_\beta|^2 - \lambda_\gamma |\nabla Y \cdot \mathbf{e}_\gamma|^2 \\ &\approx -\lambda_\gamma |\nabla Y|^2 = \frac{-\lambda_\gamma}{\rho D} \varepsilon^Y, \end{aligned} \tag{3.7}$$

where the approximation holds because the scalar gradient ∇Y is primarily aligned with the eigenvector associated with the most compressive eigenvalue, $\lambda_\gamma < 0$, as will be verified in figure 5. In addition, the coefficient of variation (standard deviation divide by mean) of both $-\lambda_\gamma$ and ρD are much smaller than that of $|\nabla Y|^2$, indicating that the relative spatial variation of the field ε^Y is minimally influenced by the coefficient $-\lambda_\gamma/\rho D$. Similarly, the connection between vortex stretching and the pseudo-dissipation rate $\varepsilon = \nu|\boldsymbol{\omega}|^2$ is

$$\boldsymbol{\omega} \cdot \mathbf{S} \cdot \boldsymbol{\omega} \approx \lambda_\beta |\boldsymbol{\omega}|^2 = \frac{\lambda_\beta}{\nu} \varepsilon \tag{3.8}$$

since vorticity is preferentially aligned with \mathbf{e}_β , and that the coefficient of variation of λ_β is smaller than that of $|\boldsymbol{\omega}|^2$.

The preferential alignment of the scalar gradient with the eigenvector corresponding to the most compressive eigenvalue is well established for passive scalars in isotropic turbulence (Batchelor 1959; Ashurst *et al.* 1987). Similarly, in RT turbulence, figure 5(a) shows that the scalar gradient ∇Y indeed aligns with the eigenvector corresponding to the most compressive eigenvalue, \mathbf{e}_γ , consistent with the findings of Cabot & Zhou (2013) in incompressible variable-density RT simulations. It indicates that ∇Y most likely aligns with \mathbf{e}_γ and is perpendicular to \mathbf{e}_β , while its alignment with \mathbf{e}_α appears more random. This alignment pattern is observed in both the low-At and mid-At cases, as well as the passive scalar in isotropic turbulence, shown in solid, dashed and dotted lines, respectively. The isotropic turbulence case corresponds to a stationary forced turbulence with passive scalar using a 512^3 grid. The alignment of vorticity with strain eigenvectors, which are shown in figure 5(b), also resembles that in incompressible isotropic turbulence, where vorticity preferentially aligns with the eigenvector \mathbf{e}_β corresponding to the intermediate eigenvalue. In figure 5(c) the PDFs of the eigenvalue ratios $\lambda_\alpha/|\lambda_\gamma|$ and $\lambda_\beta/|\lambda_\gamma|$ reveal that the most probable eigenvalue triplet $\lambda_\alpha : \lambda_\beta : \lambda_\gamma$ follows the ratio 2.84 : 1.14 : -4, close to the result of 3 : 1 : -4 reported by Ashurst *et al.* (1987). Finally, figure 5(d) shows that the vorticity field is most likely perpendicular to the scalar gradient, with $\cos(\nabla Y, \boldsymbol{\omega})$ peaking at 0. This trend is applicable to the cases of low-At, mid-At and incompressible turbulence.

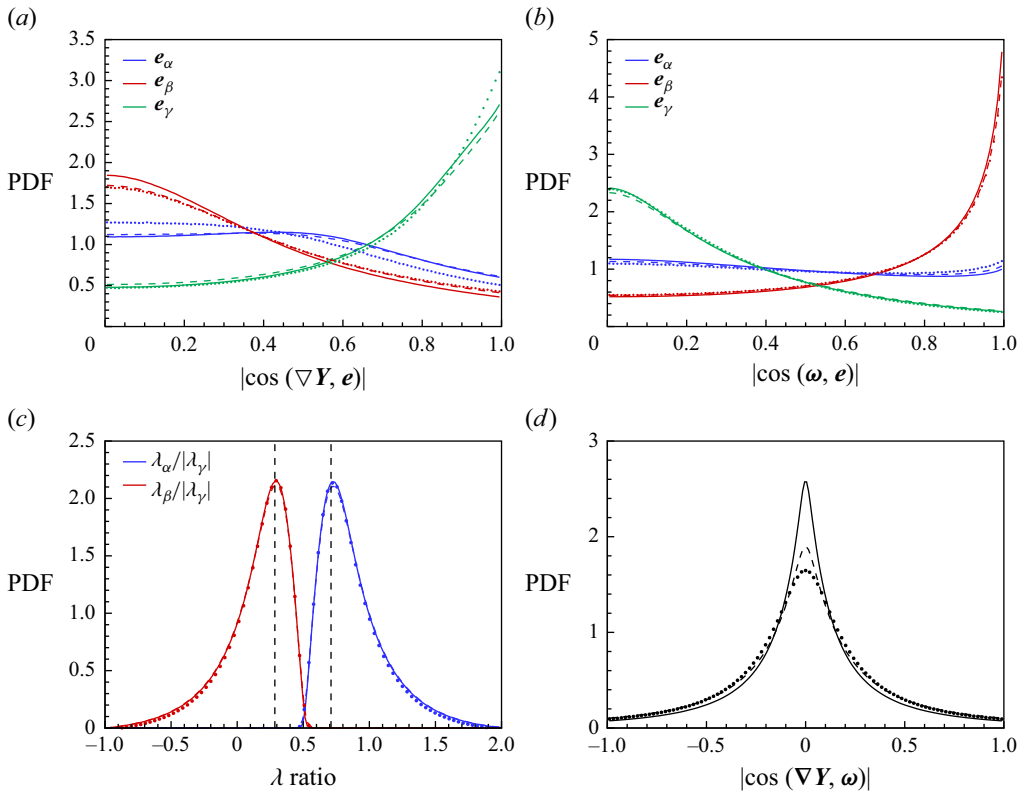


Figure 5. (a) The PDF of the absolute cosine of the angle between mass fraction gradient ∇Y and the three strain eigenvectors. (b) The PDF of the absolute cosine of the angle between vorticity ω and the strain eigenvectors. (c) The PDF of the ratios of the largest and intermediate eigenvalues, λ_α and λ_β , to the magnitude of the most compressive eigenvalue, $|\lambda_\gamma|$. The two vertical dashed lines correspond to the values of 0.285 and 0.710. (d) The PDF of the cosine value between vorticity and ∇Y . The solid, dashed and dotted lines represent the cases of low-At, mid-At, and an incompressible passive scalar turbulence, respectively.

By combining the results from figure 5 with (3.7), we observe that in developing RT turbulence, the specific alignment between the strain field and the scalar gradient links the scalar dissipation rate ε^Y to the scalar element stretching rate S^Y . This connection bridges the large-scale scalar variance $1/2\rho|Y'|^2$ with the small-scale scalar gradient magnitude $(1/2)|\nabla Y|^2$. In the following §4, we present scale decomposition to directly demonstrate that the transfer of scalar variance across length scales is equivalent to the scalar element stretching at a coarse-grained level.

3.3. Evolution of the direction of the scalar gradient

In addition to the scalar gradient magnitude, the evolution of the normal direction plays a crucial role in the alignment between ∇Y and the strain eigenframe, thereby influencing the magnitude of surface stretching term S^Y . The governing equation for the mass fraction normal vector, $\mathbf{n} = \nabla Y/|\nabla Y|$, is given by (Dopazo *et al.* 2018)

$$\frac{D}{Dt} \mathbf{n} = \underbrace{-(\mathbf{I} - \mathbf{nn}) \cdot \mathbf{S} \cdot \mathbf{n}}_{\mathcal{N}^S} + \underbrace{\frac{1}{2} \boldsymbol{\omega} \times \mathbf{n}}_{\mathcal{N}^\omega} + \underbrace{\frac{1}{|\nabla Y|} (\mathbf{I} - \mathbf{nn}) \cdot \nabla \left(\frac{1}{\rho} \nabla \cdot (\rho D \nabla Y) \right)}_{\mathcal{N}^D}. \quad (3.9)$$

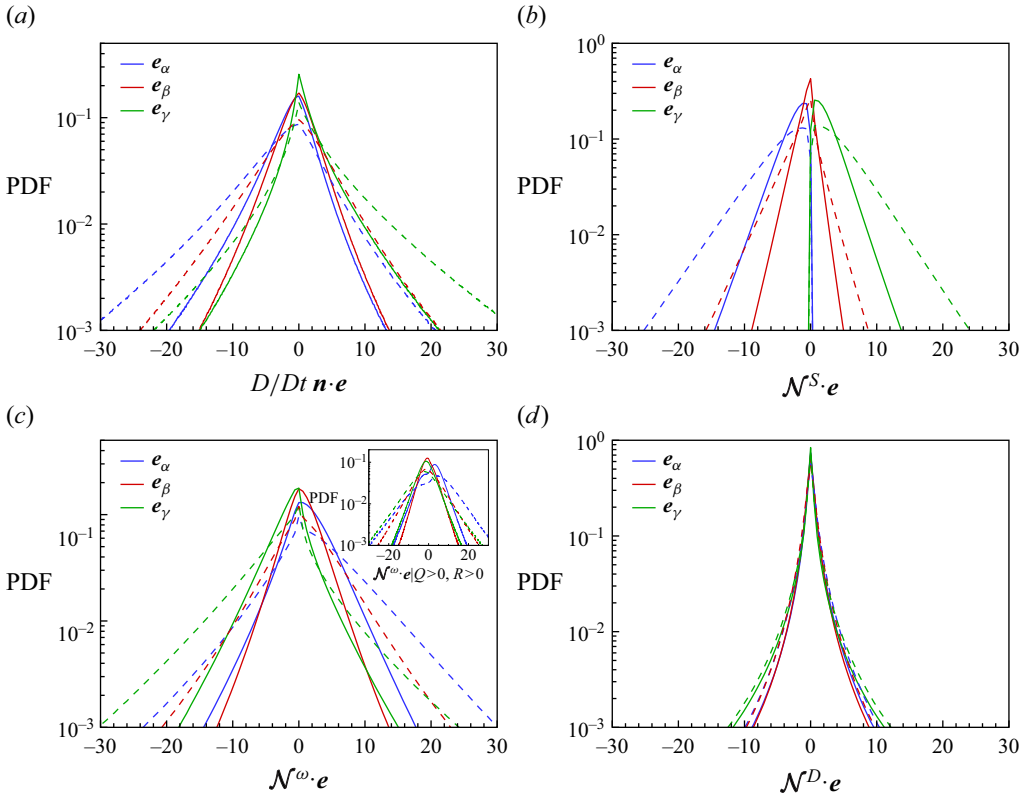


Figure 6. (a) The PDFs of the dot product between the rate of change of the scalar gradient direction and the strain eigenvectors, where the strain eigenvectors are aligned to have $\cos(\mathbf{e}, \nabla Y) \geq 0$ everywhere. (b)–(d) The individual contributions from the strain term, the vorticity term and the diffusion term on the right-hand side of (3.9). Inset of panel (c) shows the PDF of $\mathcal{N}^\omega \cdot \mathbf{e}$ conditioned on $Q > 0, R > 0$, where Q, R are the second and third invariants of the velocity gradient tensor. All panels show both the low-At (solid lines) and the mid-At (dashed lines) cases at $\hat{t} = 5$.

Unlike the evolution of the scalar gradient magnitude described in (3.4), which depends solely on the strain rate tensor in the scalar element stretching term, the evolution of the normal vector depends on both the symmetric and anti-symmetric parts of the velocity gradient tensor. The first term on the right-hand side of (3.9), \mathcal{N}^S , represents the strain-induced rotation of the normal vector on the scalar isosurface, causing it to deviate from the direction of the hydrodynamic force acting on the surface. The second term, \mathcal{N}^ω , accounts for the rotation of the normal vector due to vorticity, while the third term, \mathcal{N}^D , describes the reorientation of the normal vector related to scalar diffusion.

Figure 6 presents the contributions to the rate of change of the scalar gradient direction, illustrating the roles of different components in the preferential alignment between ∇Y and the strain eigenvectors. The total contribution is shown in panel (a), while panels (b)–(d) show the individual contributions from the terms \mathcal{N}^S , \mathcal{N}^ω and \mathcal{N}^D , respectively, at $\hat{t} = 5$ (similar results are observed at other time instants). We have aligned the eigenvectors such that $\cos(\nabla Y, \mathbf{e}) \geq 0$ everywhere, i.e. $\cos(\mathbf{n}, \mathbf{e}) = |\cos(\mathbf{n}, \mathbf{e})|$. Thus, positive values of $(D/Dt)\mathbf{n} \cdot \mathbf{e}$ indicate a tendency for ∇Y to align more strongly with the respective eigenvector, while negative values suggest a weakening of the alignment. In figure 6(a) the PDFs of $(D/Dt)\mathbf{n} \cdot \mathbf{e}$ are roughly symmetric about zero, with a slight

bias towards $(D/Dt)\mathbf{n} \cdot \mathbf{e}_\alpha < 0$ and $(D/Dt)\mathbf{n} \cdot \mathbf{e}_\gamma > 0$. This suggests that, overall, the alignment between ∇Y and the strain eigenvectors remains temporally stable, with a minor tendency to enhance the alignment between ∇Y and \mathbf{e}_γ , assuming that the rate of rotation of the strain eigenbasis is a slow process (Nomura & Post 1998) so that $(D/Dt)\mathbf{n} \cdot \mathbf{e} \approx (D/Dt)(\mathbf{n} \cdot \mathbf{e})$. This assumption has been verified numerically for both low- and mid-At cases at $\hat{t} = 5$ (not shown). For individual contributions, panel (b) reveals that $\mathcal{N}^S \cdot \mathbf{e}_\alpha < 0$ and $\mathcal{N}^S \cdot \mathbf{e}_\gamma > 0$, indicating a strong reinforcement of the preferential alignment between ∇Y and \mathbf{e}_γ . In contrast, panel (c) shows that \mathcal{N}^ω exhibits an opposite tendency, weakening the alignment between ∇Y and \mathbf{e}_γ while promoting alignment with \mathbf{e}_α . This effect is more pronounced in vorticity-dominated regions (with positive velocity gradient invariants Q and R), as highlighted in the inset of panel (c). Panel (d) shows that the diffusion term, \mathcal{N}^D , has no significant preferential contribution to any of the three eigenvectors, likely due to its passive nature. Therefore, while the strain term tends to enhance alignment between the scalar gradient and the most compressive eigenvector, the vorticity term weakens this alignment. Furthermore, figures 6(b) and 6(c) show that the PDF tails exhibit an approximate exponential decay, with fatter tails compared with the Gaussian distribution, underscoring the intermittency effect associated with RT velocity gradients.

4. Transfer of scalar variance across scales

We now examine the distribution and transfer of scalar variance across different scales. Our analysis will focus on the direction (sign) of scalar variance transfer and highlight the underlying physical mechanisms driving this process.

4.1. Filtering spectra of the velocity and scalar fields

To understand the scalar transfer across different length scales, we first analyse the distribution of KE and scalar variance among different length scales and present their spectra at various times. Since the presence of walls at the top and bottom boundaries complicates the use of a straightforward Fourier transform to decompose scales along the vertical direction, we employ the filtering spectrum proposed by Sadek & Aluie (2018). This approach defines the spectra for the KE and mass fraction fields as

$$E_{KE}(k_\ell) \equiv \frac{d}{dk_\ell} \langle \bar{\rho}_\ell |\tilde{\mathbf{u}}_\ell(\mathbf{x})|^2 \rangle / 2, \quad E_Y(k_\ell) \equiv \frac{d}{dk_\ell} \langle |\bar{Y}_\ell(\mathbf{x})|^2 \rangle / 2, \quad (4.1)$$

respectively, where $k_\ell = L_z/\ell$ is the filtering wavenumber, $\bar{f}_\ell \equiv \int G_\ell(\mathbf{r}) f(\mathbf{x} - \mathbf{r}) d\mathbf{r}$ is the spatial coarse graining and $\tilde{f}_\ell \equiv \overline{\rho f}/\bar{\rho}$ is the Favre density-weighted filtering. The filtering spectrum has been adopted in analysing 2-D and 3-D incompressible turbulence (Sadek & Aluie 2018), RT turbulence (Zhao *et al.* 2022), oceanic flows (Storer *et al.* 2022) and laser induced plasma dynamics (Yin *et al.* 2023).

Figure 7 shows the filtering spectra for KE and mass fraction at different time instants. In panel (a) the KE spectra increase over time across all scales, with their peaks gradually shifting toward lower k_ℓ , corresponding to larger scales. This behaviour, when interpreted through the Favre scale decomposition (Zhao & Aluie 2018), reflects the conversion of potential energy to KE at the largest scale, followed by a cascade of KE to progressively smaller scales driven by energy fluxes in RT turbulence (Zhao *et al.* 2022).

In contrast, the mass fraction field, whose variance is an ideal invariant with no input at any scale, behaves differently compared with KE. Figure 7 (b) shows that the spectra E_Y increase at small scales while decreasing at large scales. After $\hat{t} \geq 4$, the small-scale

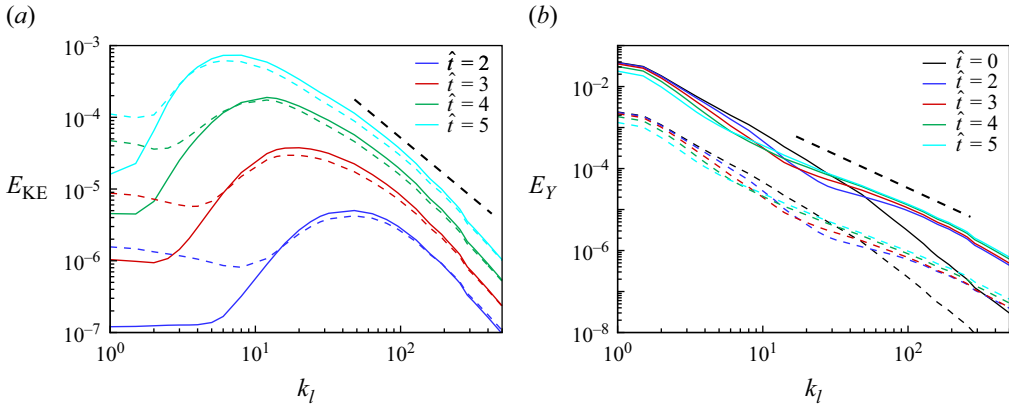


Figure 7. The filtering spectra of the (a) KE normalised by $(\rho_h - \rho_l)gL_x$ and (b) mass fraction fields for the low-At (solid lines) and mid-At (dashed lines) cases at different times. The mid-At spectra of mass fraction are shifted downwards by 1 unit to distinguish from the low-At cases. The black dashed lines represent the $k_\ell^{-5/3}$ scaling.

growth of E_Y reaches saturation, but the decrease at large scales continues. We also include E_Y at the initial instant ($\hat{t} = 0$) to illustrate the persistent trend of decreasing large-scale and increasing small-scale contents. The behaviour of E_Y is closely linked to the cross-scale transfer of mass fraction variance, as we shall discuss shortly.

4.2. Budgets of coarse-grained scalar variance and scalar gradient

Based on Favre decomposition, the budget equations for large-scale scalar variance and the scalar gradient are

$$\widetilde{\rho} \frac{D}{Dt} \frac{1}{2} \widetilde{Y}_\ell^2 = -\nabla \cdot [\widetilde{\rho} \widetilde{Y} \widetilde{\tau}(\mathbf{u}, Y) - \widetilde{Y} \overline{\rho D \nabla Y}] - \widetilde{\Pi}_\ell^Y - \overline{\varepsilon}_\ell^Y, \quad (4.2)$$

$$\widetilde{\rho} \frac{D}{Dt} \frac{1}{2} |\nabla \widetilde{Y}_\ell|^2 = -\nabla \cdot [\nabla \widetilde{Y} \nabla \cdot (\widetilde{\rho} \widetilde{\tau}(\mathbf{u}, Y))] + \widetilde{\rho} \widetilde{\mathcal{S}}_\ell^Y - \widetilde{\Pi}_\ell^{\nabla Y} - \overline{\varepsilon}_\ell^{\nabla Y}. \quad (4.3)$$

Here, $(\widetilde{D}/Dt) \equiv (\partial/\partial t) + \widetilde{\mathbf{u}}_\ell \cdot \nabla$ is the coarse-grained material derivative, $\widetilde{\Pi}_\ell^Y$ and $\widetilde{\Pi}_\ell^{\nabla Y}$ are the fluxes of scalar variance and scalar gradient, $\overline{\varepsilon}_\ell^Y$ and $\overline{\varepsilon}_\ell^{\nabla Y}$ are the coarse-grained dissipation rate of scalar and scalar gradient, $\widetilde{\mathcal{S}}_\ell^Y$ is the filtered scalar element stretching and $\widetilde{\tau}(\mathbf{u}, Y)$ is the generalised second-order moment. These terms are defined as

$$\begin{aligned} \widetilde{\Pi}_\ell^Y &= -\widetilde{\rho} \nabla \widetilde{Y} \cdot \widetilde{\tau}(\mathbf{u}, Y), \quad \widetilde{\Pi}_\ell^{\nabla Y} = -\frac{1}{\widetilde{\rho}} \nabla \cdot (\widetilde{\rho} \widetilde{\tau}(\mathbf{u}, Y)) \nabla \cdot (\widetilde{\rho} \nabla \widetilde{Y}), \\ \overline{\varepsilon}_\ell^Y &= \nabla \widetilde{Y} \cdot \overline{\rho D \nabla Y}, \quad \overline{\varepsilon}_\ell^{\nabla Y} = -\widetilde{\rho} \nabla \widetilde{Y} \cdot \nabla \left(\frac{1}{\widetilde{\rho}} \nabla \cdot \overline{\rho D \nabla Y} \right), \\ \widetilde{\mathcal{S}}_\ell^Y &= -\nabla \widetilde{Y} \cdot \nabla \widetilde{\mathbf{u}} \cdot \nabla \widetilde{Y}, \quad \widetilde{\tau}(\mathbf{u}, Y) = \widetilde{Y} \widetilde{\mathbf{u}} - \widetilde{Y} \widetilde{\mathbf{u}}. \end{aligned} \quad (4.4)$$

The coarse-grained scalar stretching $\widetilde{\mathcal{S}}_\ell^Y$ approaches the fine-grained scalar stretching \mathcal{S}^Y defined in (3.4) as ℓ approaches zero, i.e. $\lim_{\ell \rightarrow 0} \widetilde{\mathcal{S}}_\ell^Y = \mathcal{S}^Y$.

Figure 8(a) illustrates the mean values of the scalar variance flux as functions of the filtering width ℓ at different time instants. All flux terms are positive on average, indicating an overall forward transfer of scalar variance from large to small scales.

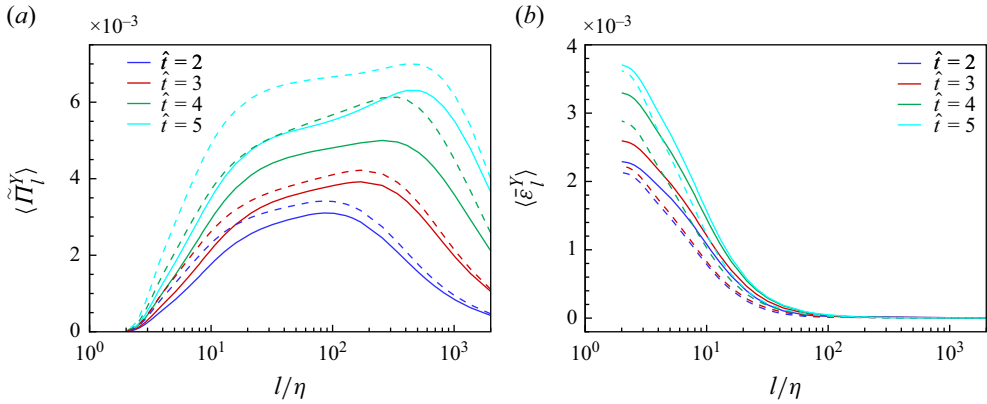


Figure 8. (a) The spatial mean values of the scalar variance flux $\tilde{\Pi}_\ell^Y$ with respect to the filtering width ℓ , normalised by the Kolmogorov scale η for both the low-At (solid lines) and mid-At (dashed lines) cases over the time interval $\hat{t} = 2-5$. (b) The mean coarse-grained scalar dissipation over scale, $\tilde{\varepsilon}_\ell^Y$.

The transfer shows a steady increase over time ($\hat{t} = 2 - 5$) as RT turbulence develops, and the length scale associated with the $\tilde{\Pi}_\ell^Y$ peak shifts towards larger scales. Since $\tilde{\Pi}_\ell^Y \equiv -\bar{\rho} \nabla \tilde{Y} \cdot \tilde{\boldsymbol{\tau}}(\mathbf{u}, Y)$ depends on both the concentration and the velocity fields, the spectra in figure 7 demonstrate that the shift of the length scale associated with the peak $\tilde{\Pi}_\ell^Y$ is mainly influenced by the velocity field. Figure 8(b) shows that the dissipation of scalar variance occurs at small length scales.

The influence of velocity fluctuations on the scalar variance flux can be manifested in its connection with the coarse-grained velocity gradient. We now explore the relationship of $\tilde{\Pi}_\ell^Y$ with the filtered velocity gradient, specifically focusing on both the strain rate and vorticity fields. The joint PDF between $\tilde{\Pi}_\ell^Y$ and the magnitude of the filtered strain rate $|\tilde{\mathbf{S}}_\ell|$ at $\ell = 64\eta$, as shown in figure 9(a), reveals a positive correlation between these two quantities. In contrast, the joint PDF between $\tilde{\Pi}_\ell^Y$ and the magnitude of the filtered vorticity $|\tilde{\boldsymbol{\omega}}_\ell|$ in figure 9(b) shows only a very weak correlation. These trends are consistent across different filtering widths, as illustrated in the conditional mean plots in figures 9(c) and 9(d). The average $\tilde{\Pi}_\ell^Y$ conditioned on $|\tilde{\mathbf{S}}_\ell|$ is a monotonically increasing function across all cases, whereas when conditioned on $|\tilde{\boldsymbol{\omega}}_\ell|$, the results are not monotonic and display significantly lower magnitudes. Overall, the findings in figure 9 suggest that the scalar variance flux $\tilde{\Pi}_\ell^Y$ is predominantly influenced by the symmetric part of the filtered velocity gradient (strain rate field) rather than the anti-symmetric part (vorticity field).

This behaviour can be well explained by the nonlinear model (Borue & Orszag 1998; Meneveau & Katz 2000b; Lees & Aluie 2019). For the moment, we equate the Favre-averaged quantities with plain spatial-averaged quantities, i.e. $\tilde{f}_\ell \approx \bar{f}_\ell$, which incurs an error of the order $O(\delta\rho/\rho) \propto O(\text{At})$ (Eyink & Drivas 2018). Based on this approximation, we have $\tilde{\boldsymbol{\tau}}(\mathbf{u}, Y) \approx \bar{\boldsymbol{\tau}}(\mathbf{u}, Y)$. By further invoking the scale-locality property (Eyink 2005) for scalar fields, $\bar{\boldsymbol{\tau}}_\ell(\mathbf{u}, Y) \approx \bar{\boldsymbol{\tau}}_\ell(\bar{\mathbf{u}}_\ell, \bar{Y}_\ell)$, and the exact identity connecting the subscale flux term for any two fields $f(\mathbf{x}), g(\mathbf{x})$ and their increments (Constantin, Weinan & Titi 1994)

$$\bar{\boldsymbol{\tau}}_\ell(f, g) = \int d^3\mathbf{r} G_\ell(\mathbf{r}) \delta f(\mathbf{x}; \mathbf{r}) \delta g(\mathbf{x}; \mathbf{r}) - \int d^3\mathbf{r} G_\ell(\mathbf{r}) \delta f(\mathbf{x}; \mathbf{r}) \int d^3\mathbf{r} G_\ell(\mathbf{r}) \delta g(\mathbf{x}; \mathbf{r}), \tag{4.5}$$

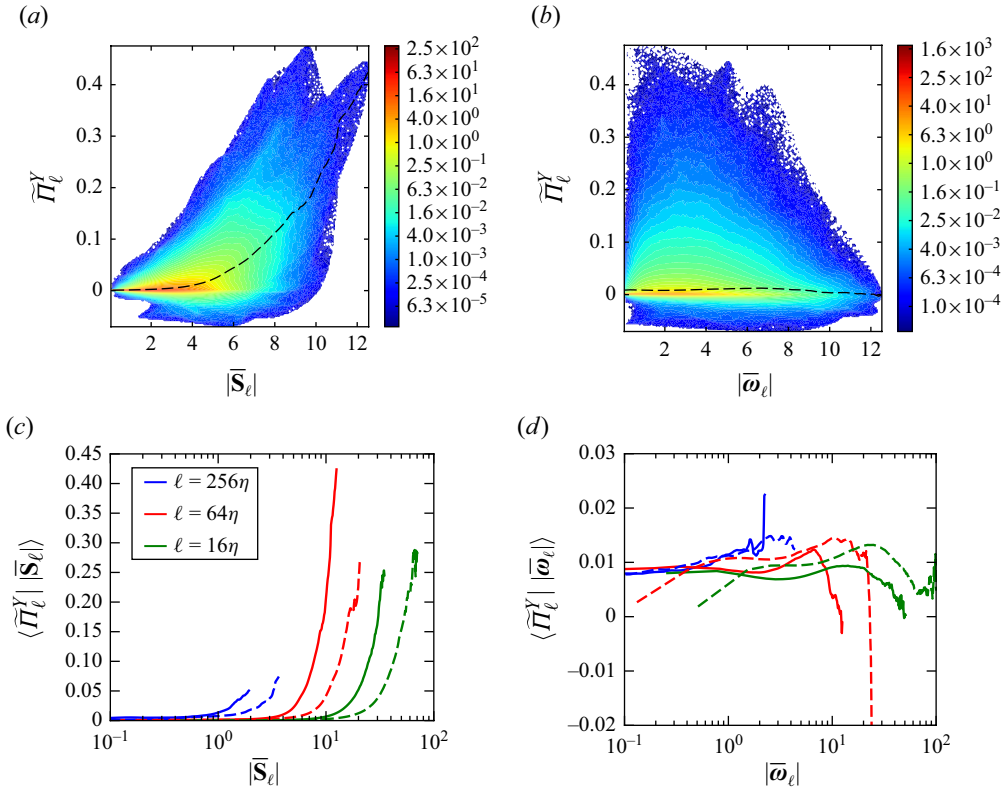


Figure 9. The correlation between scalar variance flux $\tilde{\Pi}_\ell^Y$ and the magnitude of the filtered strain rate and vorticity fields. Panels (a) and (b) show the joint PDF of $\tilde{\Pi}_\ell^Y$ with strain rate magnitude $|\bar{\mathbf{S}}|$ and vorticity magnitude $|\bar{\boldsymbol{\omega}}|$, respectively, for the low-At case at filtering width $\ell = 64\eta$ and at $\hat{t} = 5$. The black dashed lines are the conditional averaged scalar variance flux. Panels (c) and (d) are the conditional averaged $\tilde{\Pi}_\ell^Y$ at three filtering widths over $|\bar{\mathbf{S}}|$ and $|\bar{\boldsymbol{\omega}}|$, respectively. Both the low-At (solid lines) and the mid-At (dashed lines) cases at $\hat{t} = 5$ are included.

where $\delta f(\mathbf{x}; \mathbf{r}) = f(\mathbf{x} + \mathbf{r}) - f(\mathbf{x})$ and $\delta g(\mathbf{x}; \mathbf{r}) = g(\mathbf{x} + \mathbf{r}) - g(\mathbf{x})$, we have

$$\begin{aligned}
 \tilde{\Pi}_\ell^Y &= -\bar{\rho} \nabla \tilde{Y} \cdot \tilde{\boldsymbol{\tau}}(\mathbf{u}, Y) \approx -\bar{\rho} \nabla \bar{Y} \cdot \bar{\boldsymbol{\tau}}(\bar{\mathbf{Y}}, \bar{\mathbf{u}}) \\
 &= -\bar{\rho} \nabla \bar{Y} \cdot \left(\int d^3 \mathbf{r} G_\ell(\mathbf{r}) \delta \bar{Y} \delta \bar{\mathbf{u}} - \int d^3 \mathbf{r} G_\ell(\mathbf{r}) \delta \bar{Y} \int d^3 \mathbf{r} G_\ell(\mathbf{r}) \delta \bar{\mathbf{u}} \right) \\
 &\approx -\bar{\rho} \nabla \bar{Y} \cdot \left(\int d^3 \mathbf{r} G_\ell(\mathbf{r}) \mathbf{r} \cdot \nabla \bar{Y} \mathbf{r} \cdot \nabla \bar{\mathbf{u}} - \int d^3 \mathbf{r} G_\ell(\mathbf{r}) \mathbf{r} \cdot \nabla \bar{Y} \int d^3 \mathbf{r} G_\ell(\mathbf{r}) \mathbf{r} \cdot \nabla \bar{\mathbf{u}} \right) \\
 &= -\bar{\rho} \nabla \bar{Y} \cdot \ell^2 \partial_i \bar{Y} \partial_k \bar{\mathbf{u}} \int d^3 \left(\frac{\mathbf{r}}{\ell} \right) G \left(\frac{\mathbf{r}}{\ell} \right) \frac{r_i r_k}{\ell \ell} \\
 &= -C_0 \ell^2 \bar{\rho} \nabla \bar{Y} \cdot \nabla \bar{\mathbf{u}} \cdot \nabla \bar{Y} \equiv \tilde{\Pi}_{\text{NL}, \ell}^Y,
 \end{aligned} \tag{4.6}$$

where between the second the third line we have adopted the Taylor expansion $\delta \bar{Y} \approx \mathbf{r} \cdot \nabla \bar{Y}$, $\delta \bar{\mathbf{u}} \approx \mathbf{r} \cdot \nabla \bar{\mathbf{u}}$ to further approximate the expression, and the coefficient $C_0 = \int d^3 \mathbf{r} G(\mathbf{r}) |\mathbf{r}|^2$ is the second moment of the filtering kernel and, hence, is a constant. For the Gaussian kernel adopted here in (2.6), we have $C_0 = 1/12$.

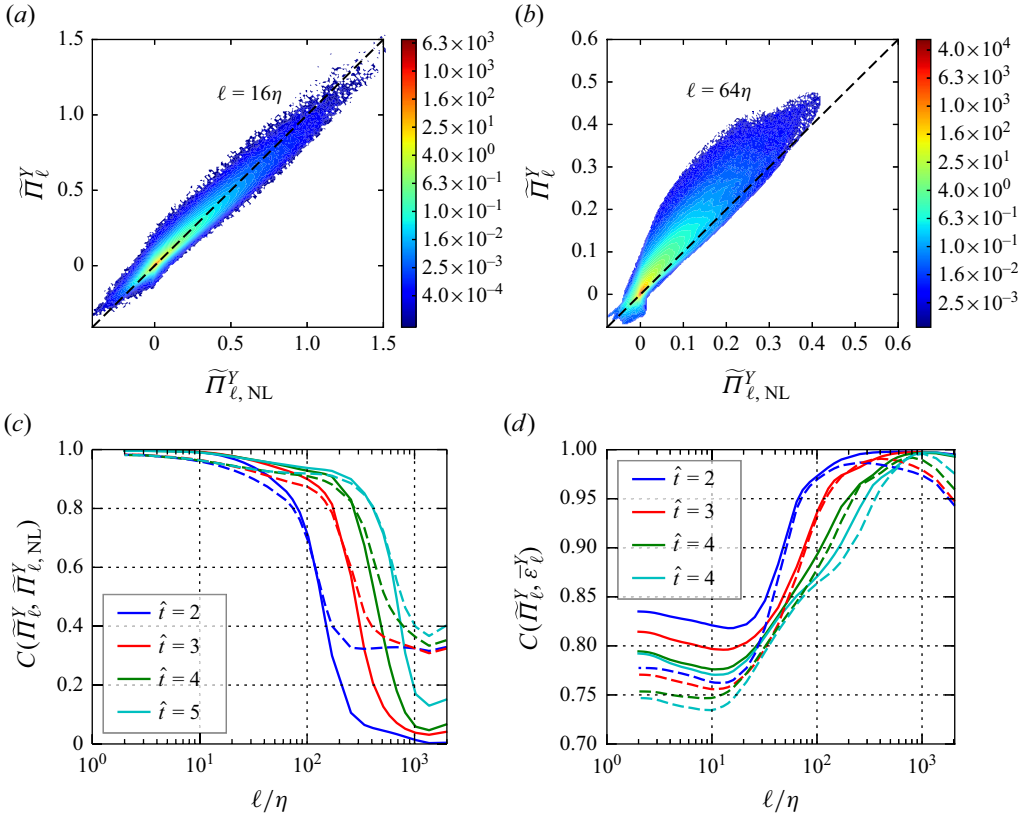


Figure 10. The joint PDF between $\tilde{\Pi}_\ell^Y$ and its nonlinear model $\tilde{\Pi}_{\ell, NL}^Y$ for the low-At case at $\hat{t} = 5$, evaluated at two widths (a) $\ell = 16\eta$ and (b) $\ell = 64\eta$. An auxiliary diagonal dashed line is included for reference. (c) The correlation coefficients between $\tilde{\Pi}_\ell^Y$ and its nonlinear model for both the low-At (solid lines) and mid-At (dashed lines) cases at $\hat{t} = 2 - 5$. (d) The correlation coefficients between $\tilde{\Pi}_\ell^Y$ and $\bar{\varepsilon}_\ell^Y$.

The nonlinear model suggests that the scalar variance flux $\tilde{\Pi}_\ell^Y$ across scale ℓ explicitly depends only on the strain rate tensor filtered at ℓ , with no direct dependence on the vorticity field. This is consistent with the conditional averaged results presented in figure 9. In deriving this model, several simplifications were made that could affect its performance. We now evaluate the model by comparing its prediction with the actual data.

Figures 10(a) and 10(b) show the joint PDF of $\tilde{\Pi}_\ell^Y$ and its nonlinear model $\tilde{\Pi}_{NL}^Y = -(1/12)\ell^2\bar{\rho}\nabla\bar{Y} \cdot \nabla\bar{u} \cdot \nabla\bar{Y}$ for the low-At case at $\hat{t} = 5$. The joint PDFs for both small and intermediate length scales, $\ell = 16\eta$ and $\ell = 64\eta$, align closely with the diagonal line, with correlation coefficients of 0.98 and 0.94, respectively. This indicates that the nonlinear model provides a strong pointwise approximation of the actual scalar variance flux.

Figure 10(c) further illustrates the correlation coefficient between the model and actual flux at different times ($\hat{t} = 2 - 5$) for both the low-At and mid-At cases. The results show that the correlation improves over time as the RT turbulence develops, suggesting that the model performs better at higher Reynolds numbers where the scale-locality assumption is applicable to a wider scale range. In addition, the correlation coefficient is higher at smaller scales, where the Taylor expansion adopted in deriving the nonlinear model is more accurate. Additionally, because of the approximation that replaces Favre-filtered quantities with plain filtered quantities, $\tilde{f}(\mathbf{x}) \rightarrow \bar{f}(\mathbf{x})$, the low-At case shows slightly

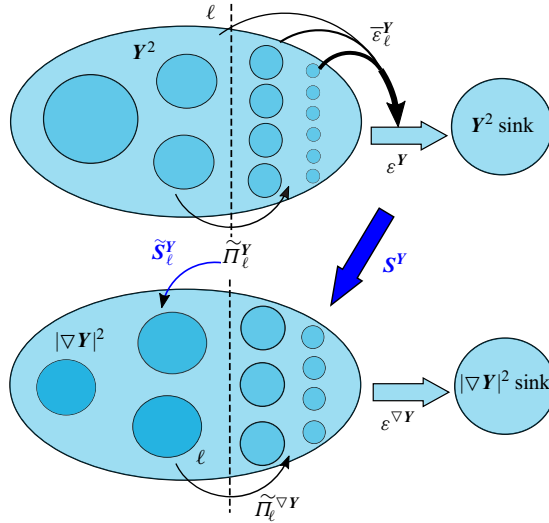


Figure 11. Schematic of the pathway of scalar variance and its gradient transfer across scales.

better correlation than the mid-At case at small to intermediate scales, due to the smaller error of the order $O(\Delta t)$. Interestingly, the correlation coefficients for the mid-At case at the largest filtering widths are slightly better than those in the low-At case, despite the overall relatively weak correlation. This trend is likely due to the higher Reynolds number in the mid-At case than the low-At case, as indicated in [table 1](#), leading to a slightly better performance of the model. In addition, the time evolution of the mean values of $\tilde{\Pi}_\ell^Y$ and $\tilde{\Pi}_{NL}^Y$, along with their correlation coefficients, are illustrated in [Appendix D](#). These results again demonstrate the good approximation of the nonlinear model within the self-similar regime of RT turbulence.

The nonlinear model $\tilde{\Pi}_{\ell,NL}^Y$ bears a strong resemblance to the filtered scalar stretching term $\tilde{S}_\ell^Y = -\partial_i \tilde{Y} \partial_j \tilde{Y} \partial_i \tilde{u}_j \approx -\partial_i \bar{Y} \partial_j \bar{Y} \partial_i \bar{u}_j = \tilde{\Pi}_{\ell,NL}^Y / (C_0 \ell^2 \bar{\rho})$. This similarity indicates a shared physical mechanism underlying both the scalar variance flux, a sink term for large-scale scalar variance in (4.2), and the filtered scalar stretching, which acts as a source term in the coarse-grained scalar gradient equation (4.3). Given that the preferential alignment between the scalar gradient and the strain eigenbasis also holds for coarse-grained fields (see [figure 13a](#)), the estimation in (3.7) that connects the fine-grained stretching term and the scalar dissipation rate is valid for the filtered results as well, i.e.

$$\tilde{\Pi}_\ell^Y \approx \tilde{\Pi}_{\ell,NL}^Y \propto \tilde{S}_\ell^Y \approx -\bar{\lambda}_\gamma |\nabla \bar{Y}_\ell|^2 \approx \frac{-\bar{\lambda}_\gamma}{\bar{\rho}_\ell D} \bar{\varepsilon}_\ell^Y \quad \text{given } \nabla \bar{Y}_\ell \parallel \mathbf{e}_\gamma, \quad (4.7)$$

where $\bar{\lambda}_\gamma$ is the eigenvalue corresponding to the most compressive eigenvector of the filtered strain field. The correlation between $\tilde{\Pi}_\ell^Y$ and the large-scale scalar dissipation $\bar{\varepsilon}_\ell^Y$ is illustrated in [figure 10\(d\)](#), where the correlation coefficients are above 0.7 at small scales, confirming the validity of (4.7). This relation reflects a form of turbulent eddy diffusivity commonly adopted in RANS or LES. Note that in [figure 10\(d\)](#) the unexpectedly high correlation between $\tilde{\Pi}_\ell^Y$ and $\bar{\varepsilon}_\ell^Y$ at large filtering scales arises from the contribution of long-wavelength modes in RT turbulence, generated by the bubble merger process. The vertical velocity and mass fraction field of these modes combine to produce a

second-order moment $\tilde{\tau}_\ell(\mathbf{u}, \mathbf{Y})$ that resembles the filtered mass fraction gradient, resulting in a strong correlation $C(\tilde{\Pi}_\ell^Y, \bar{\varepsilon}_\ell^Y) \approx 1$.

The pathways of scalar variance and scalar gradient transfer across scales and the underlying physical mechanism is depicted in [figure 11](#). At intermediate to large scales ($\gtrsim \ell$), turbulent stirring by straining motion disperses the bulk scalar field at large scale into sheet structures associated with smaller length scales, thus transferring scalar variance from large to small scales. Therefore, the strain-induced surface stretching $\tilde{\mathcal{S}}_\ell^Y$ is closely related to the transfer term $\tilde{\Pi}_\ell^Y$. On the other hand, the surface stretching $\tilde{\mathcal{S}}_\ell^Y$ acts on the tangential plane of scalar isosurfaces, accompanied by a compression in the normal direction, which brings adjacent isoscalar elements closer together and increases the coarse-grained scalar gradient $\nabla \bar{Y}_\ell$. This effect further facilitates the dissipation rate $\bar{\varepsilon}_\ell^Y$ associated with the filtered concentration field. The close proximity among $\tilde{\Pi}_\ell^Y \sim \tilde{\mathcal{S}}_\ell^Y \sim \bar{\varepsilon}_\ell^Y$ is thus established. Additionally, since $\lim_{\ell \rightarrow 0} \tilde{\mathcal{S}}_\ell^Y = \mathcal{S}^Y$ and $\lim_{\ell \rightarrow 0} \bar{\varepsilon}_\ell^Y = \varepsilon^Y$, the fine-grained quantities \mathcal{S}^Y and ε^Y also bear similarities, as shown earlier,

4.3. Backscatter of the scalar variance flux

As observed in [figures 9\(a\)](#) and [10\(a,b\)](#), while the mean value of $\tilde{\Pi}_\ell^Y$ is positive, causing a globally forward transfer of the scalar variance flux from large to small scales, locally negative values of $\tilde{\Pi}_\ell^Y$ do exist, particularly at small filtering widths ℓ , representing a backward transfer from small to large scales. [Figure 12\(a\)](#) illustrates the mean values of the positive and negative components of $\tilde{\Pi}_\ell^Y$, showing that their magnitudes increase over time for both the low-At and mid-At cases. The positive component, $\tilde{\Pi}_{\ell,+}^Y$, is significant across almost all scale ranges, whereas the negative component, $\tilde{\Pi}_{\ell,-}^Y$, is only prominent at relatively small length scales ($\ell < 160\eta$) and peaks around 16η . These results indicate that inverse scalar variance transfer predominantly occurs at small scales. Although the mean value of the negative subset of $\tilde{\Pi}_\ell^Y$ is small compared with the positive subset, the proportion of the number of $\tilde{\Pi}_{\ell,-}^Y$ samples depicted in [figure 12\(a\)](#) shows that the negative region could exceed 40 % at intermediate to small scales. This suggests that scalar variance backscatter has a widespread influence.

To gain insight into the spatial distribution and topology of the backscatter of scalar variance flux, we obtain the mean value of $\tilde{\Pi}_\ell^Y$ conditional on the $|\bar{\mathbf{S}}_\ell| - |\bar{\boldsymbol{\omega}}_\ell|$ space and the $\bar{Q}_\ell - \bar{R}_\ell$ space in [figure 12\(b\)–\(d\)](#), where $\bar{Q}_\ell \equiv -(1/2)\partial_k \bar{u}_i \partial_i \bar{u}_k$ and $\bar{R}_\ell \equiv -(1/3)\partial_j \bar{u}_i \partial_k \bar{u}_j \partial_i \bar{u}_k$ are the second and third invariants of the filtered velocity gradients. In the $|\bar{\mathbf{S}}_\ell| - |\bar{\boldsymbol{\omega}}_\ell|$ space, the negative $\tilde{\Pi}_\ell^Y$ occurs at regions with high-vorticity magnitude and low to intermediate strain magnitude, implying that vorticity plays an active role in the scalar variance backscatter. [Figure 12\(b\)](#) shows the result for the low-At case, with similar results observed for the mid-At case (not shown). In the $\bar{Q}_\ell - \bar{R}_\ell$ space shown in [figures 12\(c\)](#) and [12\(d\)](#), the conditional joint PDFs clearly show that, for both the low-At and mid-At cases, negative mean values of $\tilde{\Pi}_\ell^Y$ primarily occur in the first quadrant of the $\bar{Q}_\ell - \bar{R}_\ell$ plane, where $\bar{Q}_\ell > 0$ and $\bar{R}_\ell > 0$. This region, located above the dashed curve on the right (the Vieillefosse tail, $27/4\bar{R}_\ell^2 + \bar{Q}_\ell^3 = 0$), corresponds to the local flow pattern of vortex compression (Meneveau 2011), and that local vorticity strength dominates over strain ($\bar{Q}_\ell > 0$). Thus, the vorticity vector influences the backscatter region with $\tilde{\Pi}_\ell^Y < 0$, although its effect on the overall flux term $\tilde{\Pi}_\ell^Y$ is diminished, as indicated in the conditional mean of [figure 9\(d\)](#).

The negative scalar variance transfer is due to a modified preferential alignment between the filtered scalar gradient and the filtered strain rate eigenvectors. Due to the proximity

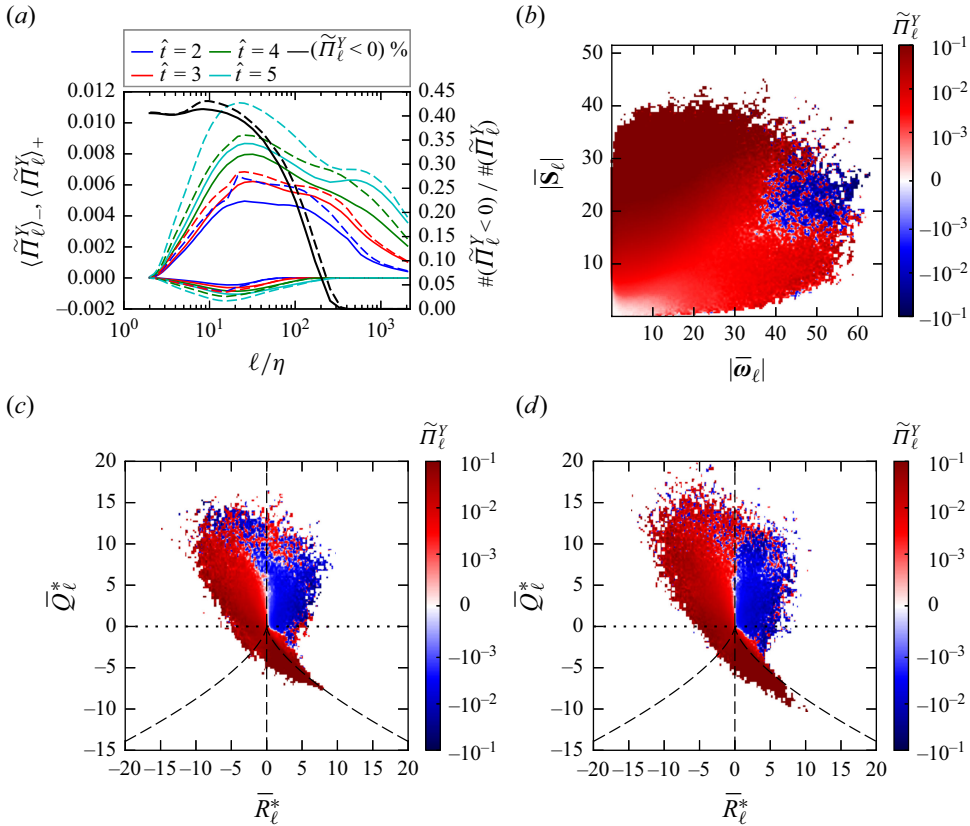


Figure 12. (a) The mean positive and negative components of the scalar variance flux, with the subscripts $\langle \cdot \rangle_+$ and $\langle \cdot \rangle_-$ indicating averages over its positive and negative subsets, respectively. The black lines represent the proportion of the negative volume of $\tilde{\Pi}_\ell^Y$ within the domain at $\hat{t} = 5$. (b) The conditional mean value $\langle \tilde{\Pi}_\ell^Y | |\bar{\mathbf{S}}_\ell|, |\bar{\boldsymbol{\omega}}_\ell| \rangle$ on the joint PDF of filtered strain and vorticity magnitudes of the low-At case at $\hat{t} = 5$, with a filtering width $\ell = 16\eta$. (c, d) The conditional mean $\langle \tilde{\Pi}_\ell^Y | \bar{Q}_\ell^*, \bar{R}_\ell^* \rangle$ for the low-At and mid-At cases at $\hat{t} = 5$ with the filtering width $\ell = 16\eta$. The second and third velocity gradient invariants \bar{Q}_ℓ and \bar{R}_ℓ are normalised by $\langle |\bar{\boldsymbol{\omega}}_\ell|^2 \rangle$ and $\langle |\bar{\boldsymbol{\omega}}_\ell|^2 \rangle^{3/2}$, respectively.

between scalar variance flux and surface stretching, we have

$$\begin{aligned} \tilde{\Pi}_\ell^Y &\propto \tilde{\mathcal{S}}^Y = -\partial_i \tilde{Y} \partial_j \tilde{Y} \tilde{\mathcal{S}}_{ij} \approx -\partial_i \bar{Y} \partial_j \bar{Y} \bar{\mathcal{S}}_{ij} \\ &= -|\nabla \bar{Y}|^2 \left(\bar{\lambda}_\alpha \cos^2(\nabla \bar{Y}, \mathbf{e}_\alpha) + \bar{\lambda}_\beta \cos^2(\nabla \bar{Y}, \mathbf{e}_\beta) + \bar{\lambda}_\gamma \cos^2(\nabla \bar{Y}, \mathbf{e}_\gamma) \right), \end{aligned} \quad (4.8)$$

where $\bar{\lambda}_\alpha, \bar{\lambda}_\beta, \bar{\lambda}_\gamma$ and $\mathbf{e}_\alpha, \mathbf{e}_\beta, \mathbf{e}_\gamma$ correspond to the eigenvalues and eigenvectors of the filtered strain rate tensor $\bar{\mathbf{S}}$, with $\bar{\lambda}_\alpha > 0$ and $\bar{\lambda}_\gamma < 0$. Thus, if $\nabla \bar{Y}$ predominantly aligns with the most compressive eigenvector \mathbf{e}_γ then $\tilde{\Pi}_\ell^Y \propto -\bar{\lambda}_\gamma |\nabla \bar{Y}|^2 \cos^2(\nabla \bar{Y}, \mathbf{e}_\gamma) > 0$. On the other hand, if $\nabla \bar{Y}$ predominantly aligns with the most expansive eigenvector \mathbf{e}_α then $\tilde{\Pi}_\ell^Y \propto -\bar{\lambda}_\alpha |\nabla \bar{Y}|^2 \cos^2(\nabla \bar{Y}, \mathbf{e}_\alpha) < 0$.

We have already shown in the scalar normal budgets (figure 6) that, for the unfiltered fields, the strain rate tensor tends to reinforce the preferential alignment between ∇Y and \mathbf{e}_γ , while the vorticity vector tends to oppose this trend and promote the alignment between ∇Y and \mathbf{e}_α . This trend persists to the filtered fields, especially at small filtering

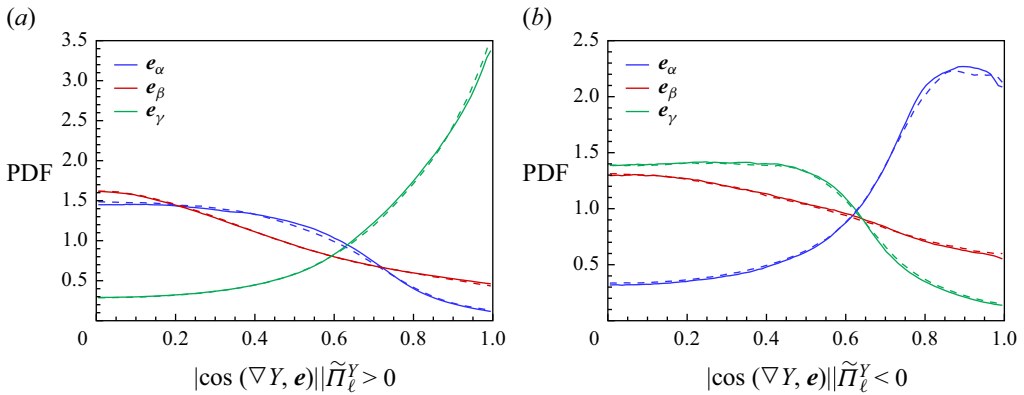


Figure 13. The alignment between the scalar gradient and the strain rate eigenvectors at $\hat{\tau} = 5$, both filtered at $\ell = 64\eta$. Panel (a) is conditional on the positive subset of $\tilde{\Pi}_\ell^Y$, while panel (b) is conditional on the negative subset. The results for both the low-At (solid lines) and mid-At (dashed lines) cases are similar.

scales where the scalar variance backscatter is most intense. Therefore, the vorticity-induced rotation of the scalar normal generates regions where $\nabla\bar{Y}$ is parallel to e_α , and hence, $\tilde{\Pi}_\ell^Y < 0$. Figures 13(a) and 13(b) show the PDFs of cosine values between $\nabla\bar{Y}_\ell$ and strain eigenvectors e filtered at $\ell = 64\eta$ and conditioned on both positive and negative $\tilde{\Pi}_\ell^Y$, respectively (comparable results are observed with other filtering widths). The PDF conditional on the forward flux in panel (a) closely resembles the unconditioned results shown in figure 5(a), where $\nabla\bar{Y}$ aligns with the most compressive eigenvector e_γ . However, when conditioned on the backscatter with $\tilde{\Pi}_\ell^Y < 0$, the best alignment occurs between $\nabla\bar{Y}$ and the most expansive eigenvector e_α . In summary, the vorticity vector rotates the scalar isosurface, generating subregions with $\nabla\bar{Y} \parallel e_\alpha$, and therefore, leads to the contraction of concentration isosurface and a negative scalar variance transfer.

5. Anisotropy in RT scalar transfer

A defining feature of RT turbulence is the persistence of anisotropy, not only in field variables like velocity and scalar gradient but also in the scalar transfer across scales. In this section we examine the directional anisotropy of $\tilde{\Pi}_\ell^Y$ at different scales and assess whether the nonlinear model accurately captures this anisotropic behaviour.

Figure 14 shows the directional anisotropy for the velocity, vorticity and scalar gradient fields at $\hat{\tau} = 5$, using the spectra of their three components. In figure 14(a) the velocity components reveal that at large and intermediate scales (small to intermediate $k_\ell \equiv L_z/\ell$), the vertical energy content is greater than the horizontal. However, at small scales, the horizontal and vertical energy contents nearly converge. Although some deviations are observed in the mid-At y components, these appear to be transient. For the vorticity spectra, a similar pattern of large-scale anisotropy and small-scale isotropy is observed, with the large-scale vertical enstrophy content being smaller than the horizontal components. A $k_\ell^{1/3}$ scaling behaviour is seen at intermediate scales, consistent with the $k_\ell^{-5/3}$ scaling in the KE spectra.

Although both the velocity and vorticity fields exhibit directional anisotropy, the anisotropy is much more pronounced in the velocity field. For the specific KE, the ratio of the total z component to the total x component is 3.9 for the low-At case and 3.6 for the mid-At case. In contrast, for the vorticity field, these ratios are 0.91 and 0.94, respectively.

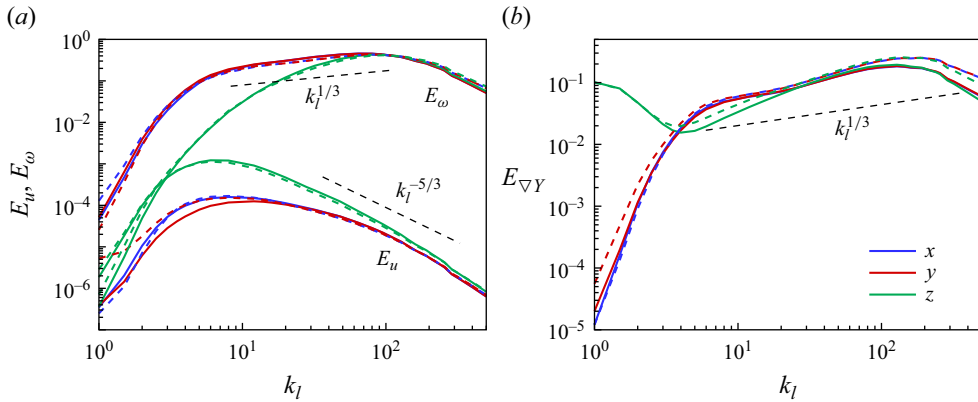


Figure 14. The filtering spectra for the (a) velocity, vorticity and (b) scalar gradient fields at $\hat{t} = 5$, where ℓ is the filtering width and $k_\ell = L_z/\ell$. Solid and dashed lines represent the low-At and mid-At cases, respectively, and black dashed lines represent the reference scalings $k_\ell^{-5/3}$, $k_\ell^{1/3}$ and $k_\ell^{1/3}$. The KE and enstrophy are normalised by the corresponding mean values.

This difference arises because small-scale components dominate the vorticity field, whereas large-scale components are more significant in the velocity field. Consequently, the small-scale isotropy of the vorticity field results in reduced directional anisotropy compared with the velocity field.

Figure 14(b) shows the spectra of the three components of the scalar gradient. The relative magnitudes of the horizontal to vertical components exhibit non-monotonic behaviour. At large scales, the vertical scalar gradient dominates due to the initial stratification, which persists at this time since the mixing region has not yet reached the walls. The z component of $E_{\nabla Y}$ then decreases with increasing k_ℓ , reaching a turning point around $k_\ell = 4$ for both the low-At and mid-At cases, a wavenumber comparable to the mixing width at $\hat{t} = 5$. Beyond this wavenumber, both horizontal and vertical components of $E_{\nabla Y}$ increase with k_ℓ , with the vertical component slightly smaller than the horizontal. The scaling appears to be slightly greater than the expected $k_\ell^{1/3}$ behaviour, which corresponds to a $k_\ell^{-5/3}$ scaling in the mass fraction spectrum. At the smallest scales, the spectra $E_{\nabla Y}$ decrease due to diffusion-induced dissipation. Overall, combining the observations from figure 14, we see that directional anisotropy persists at large scales but diminishes at smaller scales, in line with Kolmogorov’s assumption of small-scale equilibrium. In addition, the transition to isotropy occurs at larger scales (i.e. smaller transitional k_ℓ) for the scalar gradient compared with the velocity and vorticity fields.

We further investigate the anisotropy of the scalar transfer term. Figure 15(a) shows the spatial mean of the scalar variance flux components $\tilde{\Pi}_{\ell,i}^Y = -\bar{\rho}_\ell \partial_i \tilde{Y}_\ell \tilde{\tau}_\ell(Y, u_i)$, where $i = x, y$ and z . For both the low-At and mid-At cases, the z -component $\tilde{\Pi}_{\ell,z}^Y$ dominates over the horizontal components $\tilde{\Pi}_{\ell,x}^Y$ and $\tilde{\Pi}_{\ell,y}^Y$, specifically at large scales, while mean values of the two horizontal components are similar. This directional anisotropy reflects the influence of the initial density stratification and the gravitational acceleration field. The nonlinear model $\tilde{\Pi}_{\ell,NL}^Y = C_0 \ell^2 \bar{\rho} \tilde{S}_\ell^Y$, shown in figure 15(a) with open circles, is able to capture the directional anisotropy only for $\ell/\eta \lesssim 10$. However, at intermediate to large scales, the mean values of the nonlinear model deviate significantly from the simulation results, particularly for the vertical component. This deviation is expected because, for the anisotropic RT flow at relatively large scales, the assumptions underlying the nonlinear

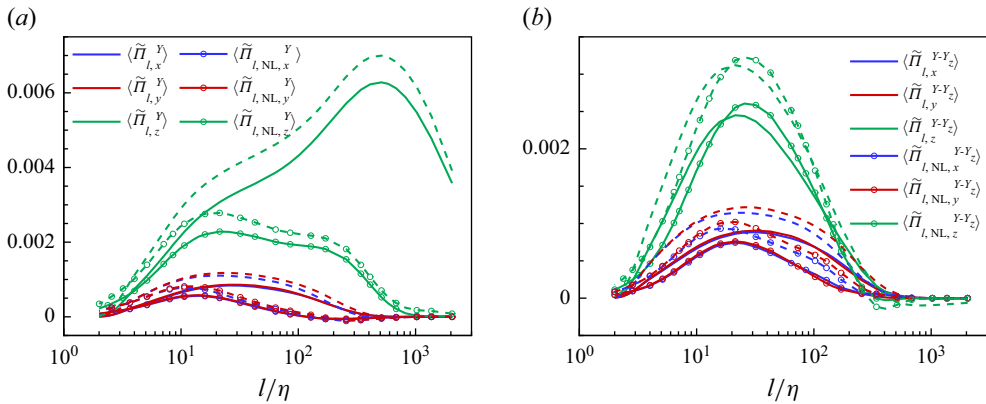


Figure 15. (a) The mean values of the three components of scalar variance transfer and the corresponding three components of the nonlinear model (marker with open circles), for both the low-At and mid-At cases at $\hat{t} = 5$. (b) Similar results, with both $\tilde{\Pi}_\ell^Y$ and its nonlinear model evaluated with the mass fraction field Y replaced by $Y - Y_z \equiv Y - \langle Y \rangle_{xy}$, i.e. subtracting the horizontal mean profile.

model, namely scale locality and the Taylor series expansion, become invalid, leading to substantial approximation errors. Potential remedies for this deviation include adopting the multi-scale gradient expansion (Eyink 2006), using higher-order Taylor expansions or employing the constant-coefficient spatial gradient model (Wang *et al.* 2022).

Without the additional complexities mentioned above, we can still enhance the performance of the nonlinear model by considering only the fluctuation part of the mass fraction field, $Y - Y_z \equiv Y - \langle Y \rangle_{xy}$. The mean vertical profile Y_z can be approximated as $Y_z \approx 1/2[1 + \text{erf}(z/h(t))]$ (Boffetta, De Lillo & Musacchio 2010), where $h(t) = \alpha At g t^2$ represents the height of the mixing width. By subtracting the mean vertical profile, we partially mitigate the dependence on the initial density stratification and reduce the external anisotropy of the system. Figure 15(b) displays the mean values of the components of $\tilde{\Pi}_\ell^Y$ and their nonlinear model for the fluctuating mass fraction field. Compared with figure 15(a), the nonlinear model provides a better approximation of the scalar variance flux, particularly for the vertical component at large scales. Thus, the nonlinear model effectively captures the directional anisotropy of $\tilde{\Pi}_\ell^{Y-Y_z}$. The remaining component, $\tilde{\Pi}^Y - \tilde{\Pi}_\ell^{Y-Y_z}$, still requires modelling, such as through the eddy viscosity model or its variants (Kokkinakis *et al.* 2015; Zhou 2017b), which we leave for future work. Figure 15 highlights the benefit of isolating the fluctuating part of the scalar field from its horizontal mean profile when developing numerical models for scalar transfer in RT turbulence.

6. Conclusions

In this paper we have investigated the multi-scale dynamics of scalar mixing in RT turbulence for low ($At = 0.15$) and moderate ($At = 0.5$) Atwood number cases. The scalar variance flux across scales, $\tilde{\Pi}_\ell^Y$, is on average positive, thus transfers scalar variance from large to small scales. A nonlinear model of $\tilde{\Pi}_\ell^Y$ shows that its magnitude depends primarily on the symmetric strain rate tensor, rather than the vorticity fields. However, locally, the scalar variance flux can become negative, partly due to vorticity-induced alignment of the scalar normal direction with the most expansive eigenvector of the strain field. Therefore, while the symmetric velocity gradient primarily influences the magnitude of $\tilde{\Pi}_\ell^Y$, the anti-symmetric velocity gradient also contributes to generating negative values of $\tilde{\Pi}_\ell^Y$. Similar

results are also observed in simulations with high Atwood and high Reynolds numbers. Additionally, we demonstrate the directional anisotropy in RT turbulence, showing that the nonlinear model accurately captures the anisotropic behaviour of the scalar transfer term when focusing on the fluctuating component of the scalar field, with the horizontal mean profile subtracted.

In the temporal evolution of RT mixing, we observe that during the self-similar stage, the statistics of various kinematic and dynamical quantities remain stable over time. For instance, the interfacial area of the scalar isosurface increases linearly with time, while the fractal dimensions of the isosurface fluctuate around 2.41 for the low-At case and 2.46 for the mid-At case. The change in isosurface area is primarily governed by the scalar element stretching, \mathcal{S}^Y . Furthermore, we establish a similarity between \mathcal{S}^Y and the mean scalar dissipation, ε^Y , through the preferential alignment of the scalar normal with the eigenvector corresponding to the most compressive eigenvalue of the strain field. This alignment is shown to be reinforced by the rate of change of the scalar normal direction due to the straining term, while the vorticity term tends to weaken this alignment.

The evolution of the scalar field is further investigated using a spatial coarse-graining approach to analyse the cross-scale transfer of scalar variance, in particular the transfer term $\tilde{\Pi}_\ell^Y \equiv -\bar{\rho}\partial_j\tilde{Y}\tilde{\tau}(Y, u_j)$. Numerical results show that the spatial mean of $\tilde{\Pi}_\ell^Y$ is consistently positive, indicating a downscale transfer of scalar variance. The conditional mean analysis reveals that $\tilde{\Pi}_\ell^Y$ is positively correlated with the filtered strain, with no significant correlation with the filtered vorticity field. This behaviour is well captured by the nonlinear model $\tilde{\Pi}_\ell^Y \approx \tilde{\Pi}_{\ell, \text{NL}}^Y = -C_0\ell^2\bar{\rho}\nabla\bar{Y} \cdot \bar{\mathbf{S}} \cdot \nabla\bar{Y} \approx C_0\ell^2\bar{\rho}\tilde{\mathcal{S}}^Y$, which is validated through joint PDFs and correlation coefficients.

Additionally, the role of vorticity in scalar transfer is primarily associated with the negative values of $\tilde{\Pi}_\ell^Y$, which indicate an inverse transfer from small to large scales. These negative values are predominantly found in the first quadrant of the filtered $\bar{Q}_\ell - \bar{R}_\ell$ space, where vorticity is dominant. Furthermore, negative $\tilde{\Pi}_\ell^Y$ is due to changes in the preferential alignment statistics between $\nabla\bar{Y}_\ell$ and the strain eigensystem. While the overall statistics indicate that $\nabla\bar{Y}$ is mostly parallel to \mathbf{e}_γ , the results conditional on negative $\tilde{\Pi}_\ell^Y$ reveal an alignment between $\nabla\bar{Y}$ and \mathbf{e}_α . This shift in alignment is attributed to the vorticity-induced rotation of the scalar normal direction, resulting in negative scalar stretching, $\mathcal{S}_\ell^Y < 0$, which in turn leads to negative $\tilde{\Pi}_\ell^Y$. Thus, both the strain rate and vorticity fields play crucial roles in influencing scalar variance transfer across scales.

Finally, we investigate the directional anisotropy in RT turbulence, specifically focusing on the anisotropy of the scalar transfer term. A key finding is that directional anisotropy is pronounced at large scales but diminishes at smaller scales. The scalar variance transfer displays significant anisotropy among its components, and the nonlinear model fails to capture this behaviour. However, when the horizontally averaged profile of the mass fraction is subtracted, the directional anisotropy decreases, leading to improved predictions from the nonlinear model. Therefore, it is beneficial to treat the horizontally averaged mass fraction profile and the fluctuating component separately when modelling RT scalar mixing.

Funding. This work is supported by the National Natural Science Foundation of China (Nos. 12202270, 12102258 and 12372264), and the China Postdoctoral Science Foundation (No. 2023M742269). The authors also appreciate the computational support from the Centre for High Performance Computing at Shanghai Jiao Tong University.

Declaration of interests. The authors report no conflict of interest.

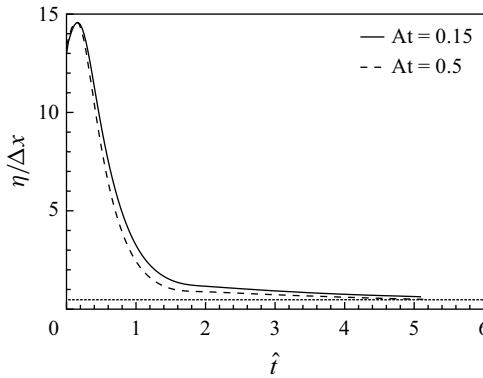


Figure 16. Temporal evolution of the Kolmogorov scale, η , normalised by the grid size Δx . The dotted line marks the threshold for an adequate resolution of the small scales in turbulent flows, $\eta/\Delta x = 1.5/\pi$, or $k_{\max}\eta \geq 1.5$, where k_{\max} is the maximum resolved wavenumber.

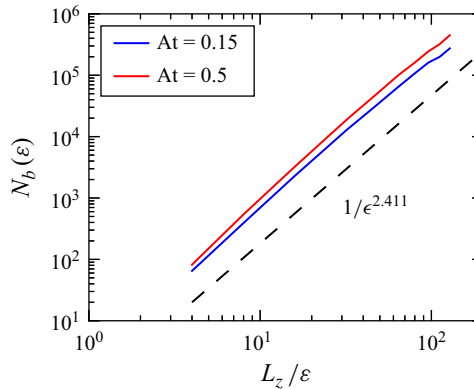


Figure 17. The fractal dimensions for the low-At and mid-At $Y = 0.5$ isosurfaces determined using the box-counting algorithm. Here, ε represents the box size and $N_b(\varepsilon)$ is the total number of boxes required to fully cover the isosurface with non-overlapping boxes of size ε . The scaling exponents D_3 represent the fractal dimensions of the isosurfaces embedded in 3-D space, calculated to be 2.411 for the low-At case and 2.474 for the mid-At case.

Appendix A. Temporal evolution of the Kolmogorov scale in RT simulations

Figure 16 shows the evolution of the Kolmogorov scale, η , defined in table 1, normalised by the grid size. In both the low-At and mid-At cases, η exhibits a sharp decrease before $\hat{t} < 1$. After this point, the rate of decrease slows and gradually stabilises after $\hat{t} > 2$, corresponding to the self-similar stage of RT evolution, as indicated in figure 2. Throughout the entire evolution, the criterion $k_{\max}\eta \geq 1.5$ is met in both simulations, ensuring sufficient resolution to capture the small turbulent scales (Yeung & Pope 1989).

Appendix B. Fractal dimension of isoscalar surfaces

Figure 17 illustrates the application of the box-counting algorithm to determine fractal dimension, D_3 , of the $Y = 0.5$ isosurface shown in figure 3. The algorithm partitions the 3-D space into non-overlapping cubes of varying sizes, ε . For each partition with a fixed ε , the total number of cubes required to fully cover the isoscalar surface is denoted

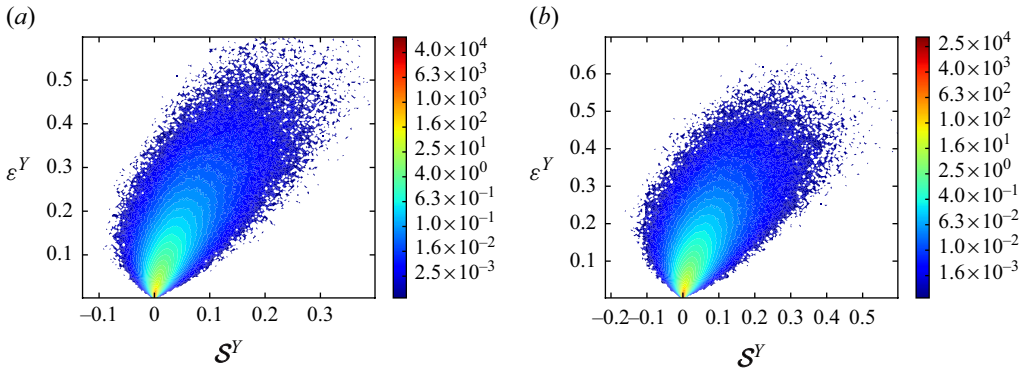


Figure 18. The joint PDFs between the scalar stretching S^Y and scalar dissipation ε^Y at $\hat{t} = 5$ for the (a) low-At and (b) mid-At cases. Both the S^Y and ε^Y fields are normalised by their respective maximum value.

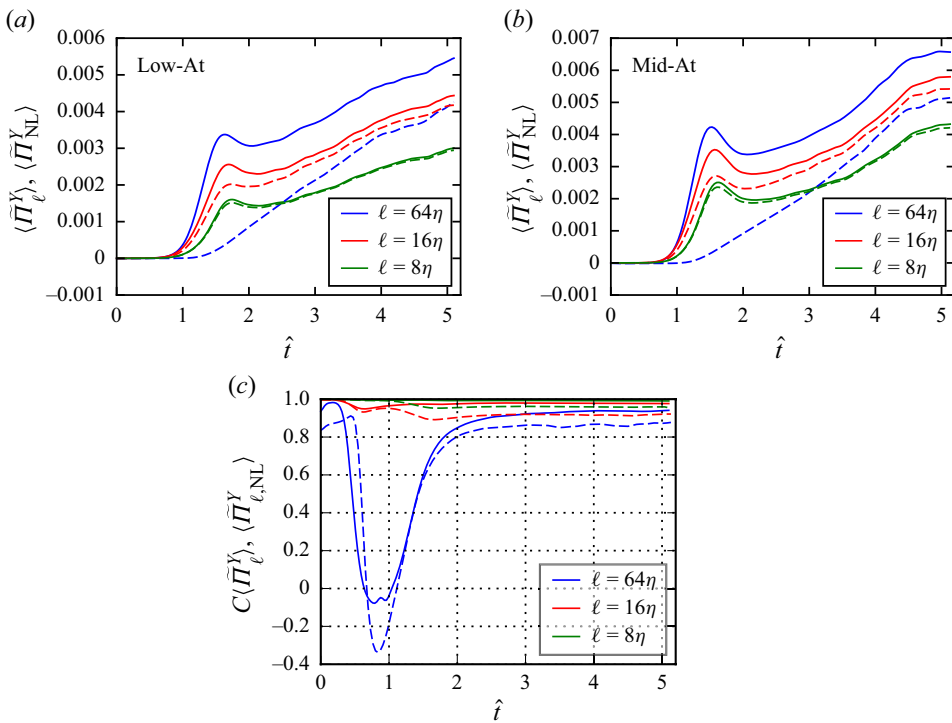


Figure 19. (a) Temporal evolution of the mean scalar variance flux and its nonlinear model for the low-At case, where solid lines represent $\langle \Pi_\ell^Y \rangle$ and dashed lines represent $\langle \Pi_{NL}^Y \rangle$. Panel (b) presents similar results for the mid-At case. Panel (c) shows the correlation coefficients between $\langle \Pi_\ell^Y \rangle$ and $\langle \Pi_{NL}^Y \rangle$, with solid and dashed lines corresponding to the low-At and mid-At cases, respectively.

as $N_b(\varepsilon)$. If the isosurface exhibits self-similar fractal characteristics, the relationship $N_b(\varepsilon) \sim (1/\varepsilon)^{D_3}$ holds, allowing the determination of the fractal dimension D_3 of the isosurface within the 3-D space.

Figure 17 shows that the isosurfaces for both the low-At and mid-At cases at $\hat{t} = 5$ are self-similar, with fractal dimensions of 2.411 and 2.474, respectively. The slightly higher

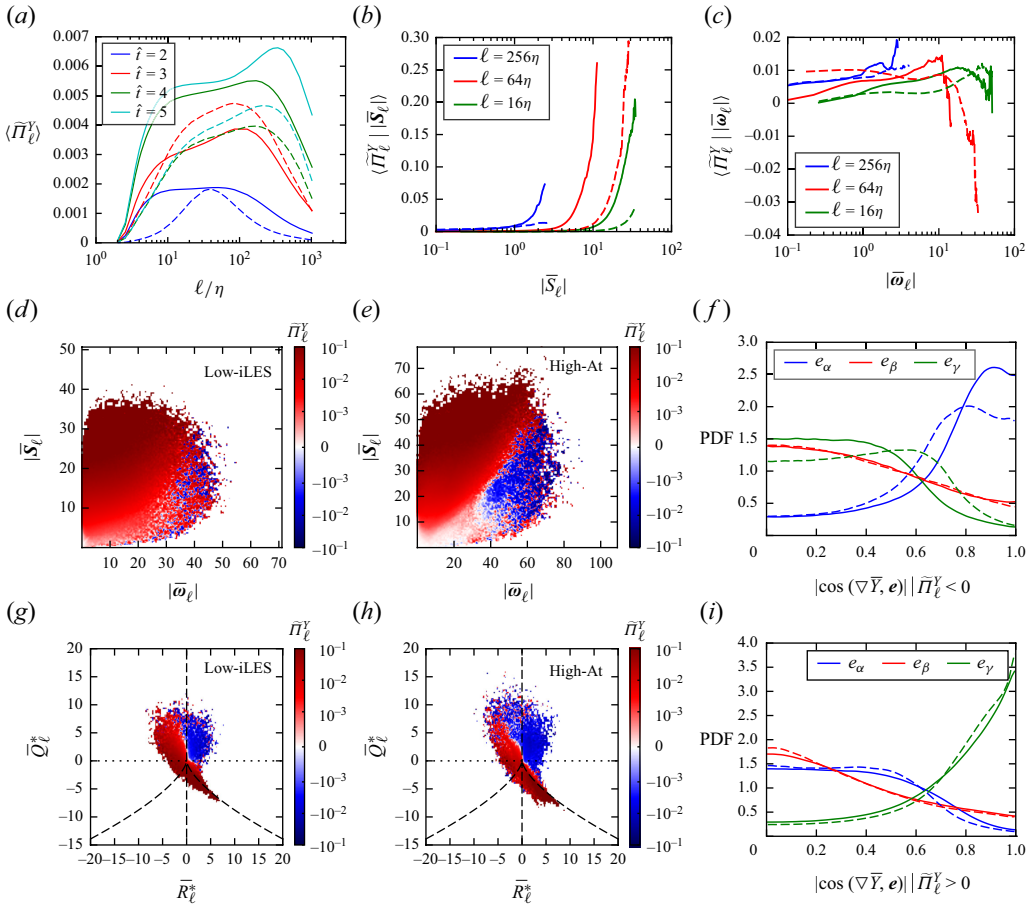


Figure 20. Scalar variance transfer statistics for the low-iLES (solid lines) and high-At (dashed lines) cases are presented. Panel (a) shows the mean value of the scalar variance transfer term over filter widths at $\hat{t} = 2 - 5$. Panels (b) and (c) show the mean value of $\tilde{\Pi}_\ell^Y$ conditioned on the filtered strain rate and vorticity magnitudes, respectively. Panels (d, e) and (g, h) show the mean value of $\tilde{\Pi}_\ell^Y$ conditioned on the joint PDFs of $|\bar{S}_\ell| - |\bar{\omega}_\ell|$ and $\bar{Q}_\ell - \bar{R}_\ell$, respectively, for both the low-iLES and high-At cases. Finally, (f) and (i) illustrate the alignment between the filtered scalar gradient and the strain rate eigensystem for the negative and positive portions of $\tilde{\Pi}_\ell^Y$. The results in panels (b)–(i) are obtained at $\hat{t} = 5$.

fractal dimension of the mid-At isosurface corresponds to the larger surface area shown in figure 2(a), indicating a more corrugated surface due to the larger density contrast and greater potential energy release in the mid-At case.

Appendix C. Correlation between surface stretching and scalar dissipation

In addition to the correlation between the temporal evolution of spatial mean values of surface stretching \mathcal{S}^Y and scalar dissipation ε^Y shown in figure 4, there is also a spatial correlation, as depicted in figure 18, with correlation coefficients of 0.95 and 0.93 for the low-At and mid-At cases, respectively. This high correlation arises from the preferential alignment between ∇Y and e_γ , as indicated in (3.7).

Appendix D. Temporal evolution of the nonlinear model prediction

To further evaluate the nonlinear model approximation of the scalar variance flux, complementing the results in figure 10, we present the temporal evolution of the mean scalar variance flux and its nonlinear model in figures 19(a) and 19(b), along with the correlation coefficient between the two in figure 19(c). The results show that for both low- and mid-At cases, $\langle \Pi_{\text{NL}}^Y \rangle$ approaches $\langle \Pi_\ell^Y \rangle$ as the filter width decreases. Additionally, the correlation coefficient between the flux and the nonlinear model remains above 0.8 for $\hat{t} > 2$, when RT turbulence is in the self-similar regime. These findings, presented in figure 19, further confirm the nonlinear model's good approximation of the scalar variance flux in RT turbulence.

Appendix E. The case of high Atwood and high Reynolds numbers

In this section we demonstrate that the main findings of the paper are applicable to both high Atwood number and high Reynolds number RT turbulence. Statistics of the scalar variance transfer term, $\tilde{\Pi}_\ell^Y$, for the high-At and low-iLES cases, as detailed in table 1, are shown in figure 20. The results confirm that the mean value of $\tilde{\Pi}_\ell^Y$ is positive and positively correlated with the filtered strain rate tensor. The negative portion of $\tilde{\Pi}_\ell^Y$ is correlated with high-vorticity regions and is associated with a modified alignment between the scalar gradient and the filtered strain rate eigensystem, where an alignment between $\nabla \bar{Y}_\ell$ and \mathbf{e}_α is observed in regions of negative $\tilde{\Pi}_\ell^Y$.

REFERENCES

- ABARZHI, S.I. 2010a On fundamentals of Rayleigh–Taylor turbulent mixing. *EPL (Europhys. Lett.)* **91** (3), 35001.
- ABARZHI, S.I. 2010b Review of theoretical modelling approaches of Rayleigh–Taylor instabilities and turbulent mixing. *Philos. Trans. R. Soc. A* **368**(1916), 1809–1828.
- AMENDT, P., COLVIN, J.D., TIPTON, R.E., HINKEL, D.E., EDWARDS, M.J., LANDEN, O.L., RAMSHAW, J.D., SUTER, L.J., VARNUM, W.S. & WATT, R.G. 2002 Indirect-drive noncryogenic double-shell ignition targets for the national ignition facility: design and analysis. *Phys. Plasmas* **9** (5), 2221–2233.
- ASHURST, W.T. 1996 Flame propagation along a vortex: the baroclinic push. *Combust. Sci. Technol.* **112** (1), 175–185.
- ASHURST, W.T., KERSTEIN, A.R., KERR, R.M. & GIBSON, C.H. 1987 Alignment of vorticity and scalar gradient with strain rate in simulated Navier–Stokes turbulence. *Phys. Fluids* **30** (8), 2343–2353.
- BANERJEE, A. 2020 Rayleigh–Taylor instability: a status review of experimental designs and measurement diagnostics. *J. Fluids Engng* **142** (12), 120801.
- BANERJEE, A. & ANDREWS, M.J. 2009 3D simulations to investigate initial condition effects on the growth of Rayleigh–Taylor mixing. *Intl J. Heat Mass Transfer* **52** (17–18), 3906–3917.
- BATCHELOR, G.K. 1952 The effect of homogeneous turbulence on material lines and surfaces. *Proc. R. Soc. Lond. A* **213**(1114), 349–366.
- BATCHELOR, G.K. 1959 Small-scale variation of convected quantities like temperature in turbulent fluid. Part 1. General discussion and the case of small conductivity. *J. Fluid Mech.* **5** (1), 113–133.
- BETTI, R. & HURRICANE, O.A. 2016 Inertial-confinement fusion with lasers. *Nat. Phys.* **12** (5), 435.
- BIFERALE, L., MANTOVANI, F., SBRAGAGLIA, M., SCAGLIARINI, A., TOSCHI, F. & TRIPICCIONE, R. 2010 High resolution numerical study of Rayleigh–Taylor turbulence using a thermal lattice Boltzmann scheme. *Phys. Fluids* **22** (11), 115112.
- BOFFETTA, G., DE LILLO, F. & MUSACCHIO, S. 2010 Nonlinear diffusion model for Rayleigh–Taylor mixing. *Phys. Rev. Lett.* **104** (3), 034505.
- BOFFETTA, G. & MAZZINO, A. 2017 Incompressible Rayleigh–Taylor turbulence. *Annu. Rev. Fluid Mech.* **49**, 119–143.
- BOFFETTA, G., MAZZINO, A., MUSACCHIO, S. & VOZELLA, L. 2009 Kolmogorov scaling and intermittency in Rayleigh–Taylor turbulence. *Phys. Rev. E* **79** (6), 065301.
- BORUE, V. & ORSZAG, S.A. 1998 Local energy flux and subgrid-scale statistics in three-dimensional turbulence. *J. Fluid Mech.* **366**, 1–31.

- BRADY, P.T. & LIVESCU, D. 2019 High-order, stable, and conservative boundary schemes for central and compact finite differences. *Comput. Fluids* **183**, 84–101.
- BUTTNER, W.T., WILLIAMS, R.J.R. & NAJJAR, F.M. 2017 Foreword to the special issue on ejecta. *J. Dyn. Behav. Mater.* **3**, 151–155.
- CABOT, W. & ZHOU, Y. 2013 Statistical measurements of scaling and anisotropy of turbulent flows induced by Rayleigh–Taylor instability. *Phys. Fluids* **25** (1), 015107.
- CABOT, W.H. & COOK, A.W. 2006 Reynolds number effects on Rayleigh–Taylor instability with possible implications for type Ia supernovae. *Nat. Phys.* **2** (8), 562–568.
- CAMPBELL, E.M. *et al.* 2021 Direct-drive laser fusion: status, plans and future. *Phil. Trans. R. Soc. Lond. A* **379**, 20200011.
- CHEN, F., XU, A. & ZHANG, G. 2018 Collaboration and competition between Richtmyer–Meshkov instability and Rayleigh–Taylor instability. *Phys. Fluids* **30** (10), 102105.
- CHEN, J., XU, A., CHEN, D., ZHANG, Y. & CHEN, Z. 2022 Discrete Boltzmann modeling of Rayleigh–Taylor instability: effects of interfacial tension, viscosity, and heat conductivity. *Phys. Rev. E* **106** (1), 015102.
- CHERTKOV, M. 2003 Phenomenology of Rayleigh–Taylor turbulence. *Phys. Rev. Lett.* **91** (11), 115001.
- CLARK, R.A., FERZIGER, J.H. & REYNOLDS, W.C. 1979 Evaluation of subgrid-scale models using an accurately simulated turbulent flow. *J. Fluid Mech.* **91** (1), 1–16.
- CONSTANTIN, P., WEINAN, E. & TITI, E.S. 1994 Onsager’s conjecture on the energy conservation for solutions of Euler’s equation. *Commun. Math. Phys.* **165** (1), 207–209.
- COOK, A.W., CABOT, W. & MILLER, P.L. 2004 The mixing transition in Rayleigh–Taylor instability. *J. Fluid Mech.* **511**, 333–362.
- COOK, A.W. & ZHOU, Y. 2002 Energy transfer in Rayleigh–Taylor instability. *Phys. Rev. E* **66** (2), 026312.
- CUI, A. & STREET, R.L. 2004 Large-eddy simulation of coastal upwelling flow. *Environ. Fluid Mech.* **4**, 197–223.
- DANAÏLA, L., ANSELMET, F., LE GAL, P., DUSEK, J., BRUN, C. & PUMIR, A. 1997 Predictions of small-scale statistics for a passive scalar in turbulent mixing. *Phys. Rev. Lett.* **79** (23), 4577.
- DIMONTE, G. *et al.* 2004 A comparative study of the turbulent Rayleigh–Taylor instability using high-resolution three-dimensional numerical simulations: the alpha-group collaboration. *Phys. Fluids* **16** (5), 1668–1693.
- DOPAZO, C., MARTIN, J., CIFUENTES, L. & HIERRO, J. 2018 Strain, rotation and curvature of non-material propagating iso-scalar surfaces in homogeneous turbulence. *Flow Turbul. Combust.* **101**, 1–32.
- EYINK, G.L. 2005 Locality of turbulent cascades. *Physica D* **207** (1), 91–116.
- EYINK, G.L. 2006 Multi-scale gradient expansion of the turbulent stress tensor. *J. Fluid Mech.* **549**, 159–190.
- EYINK, G.L. & DRIVAS, T.D. 2018 Cascades and dissipative anomalies in compressible fluid turbulence. *Phys. Rev. X* **8** (1), 011022.
- GAUTHIER, S. 2017 Compressible Rayleigh–Taylor turbulent mixing layer between Newtonian miscible fluids. *J. Fluid Mech.* **830**, 211–256.
- GAUTHIER, S. & LE CREURER, B. 2010 Compressibility effects in Rayleigh–Taylor instability-induced flows. *Phil. Trans. R. Soc. Lond. A* **368** (1916), 1681–1704.
- HASEGAWA, S., NISHIHARA, K. & SAKAGAMI, H. 1996 Numerical simulation of mixing by Rayleigh–Taylor instability and its fractal structures. *Fractals* **4** (03), 241–250.
- HE, X., CHEN, S. & ZHANG, R. 1999 A lattice Boltzmann scheme for incompressible multiphase flow and its application in simulation of Rayleigh–Taylor instability. *J. Comput. Phys.* **152** (2), 642–663.
- HILLEBRANDT, W. & NIEMEYER, J.C. 2000 Type Ia supernova explosion models. *Annu. Rev. Astron. Astrophys.* **38** (1), 191–230.
- IYER, K.P. & YEUNG, P.K. 2014 Structure functions and applicability of Yaglom’s relation in passive-scalar turbulent mixing at low Schmidt numbers with uniform mean gradient. *Phys. Fluids* **26** (8), 085107.
- KEENAN, J.J., MAKAROV, D.V. & MOLKOV, V.V. 2014 Rayleigh–Taylor instability: modelling and effect on coherent deflagrations. *Int. J. Hydrogen Energy* **39** (35), 20467–20473.
- KOKKINAKIS, I.W., DRIKAKIS, D., YOUNGS, D.L. & WILLIAMS, R.J.R. 2015 Two-equation and multi-fluid turbulence models for Rayleigh–Taylor mixing. *Int. J. Heat Fluid Flow* **56**, 233–250.
- KRASNOPOLSKAYA, T.S., MELESHKO, V.V., PETERS, G.W.M. & MEIJER, H.E.H. 1999 Mixing in stokes flow in an annular wedge cavity. *Eur. J. Mech. B Fluids* **18** (5), 793–822.
- LAI, H., XU, A., ZHANG, G., GAN, Y., YING, Y. & SUCCI, S. 2016 Nonequilibrium thermohydrodynamic effects on the Rayleigh–Taylor instability in compressible flows. *Phys. Rev. E* **94** (2), 023106.
- LEES, A. & ALUIE, H. 2019 Baropycnal work: a mechanism for energy transfer across scales. *Fluids* **4** (2), 92.
- LELE, S.K. 1992 Compact finite difference schemes with spectral-like resolution. *J. Comput. Phys.* **103** (1), 16–42.

- LIANG, H., LI, Q.X., SHI, B.C. & CHAI, Z.H. 2016 Lattice Boltzmann simulation of three-dimensional Rayleigh–Taylor instability. *Phys. Rev. E* **93** (3), 033113.
- LINDEN, P.F., REDONDO, J.M. & YOUNGS, D.L. 1994 Molecular mixing in Rayleigh–Taylor instability. *J. Fluid Mech.* **265**, 97–124.
- LIU, Z., SONG, J., XU, A., ZHANG, Y. & XIE, K. 2023 Discrete Boltzmann modeling of plasma shock wave. *Proc. Inst. Mech. Engrs C: J. Mech. Engng Sci.* **237** (11), 2532–2548.
- LIVESCU, D. 2013 Numerical simulations of two-fluid turbulent mixing at large density ratios and applications to the Rayleigh–Taylor instability. *Phil. Trans. R. Soc. Lond. A* **371**(2003), 20120185.
- LIVESCU, D. 2020 Turbulence with large thermal and compositional density variations. *Annu. Rev. Fluid Mech.* **52**, 309–341.
- LIVESCU, D. & RISTORCELLI, J.R. 2007 Buoyancy-driven variable-density turbulence. *J. Fluid Mech.* **591**, 43–71.
- LIVESCU, D. & RISTORCELLI, J.R. 2008 Variable-density mixing in buoyancy-driven turbulence. *J. Fluid Mech.* **605**, 145–180.
- LIVESCU, D., RISTORCELLI, J.R., GORE, R.A., DEAN, S.H., CABOT, W.H. & COOK, A.W. 2009 High-Reynolds number Rayleigh–Taylor turbulence. *J. Turbul.* **10**, N13.
- LORENSEN, W.E. & CLINE, H.E. 1998 Marching cubes: a high resolution 3D surface construction algorithm. In *Seminal Graphics: Pioneering Efforts that Shaped the Field*, pp. 347–353. Association for Computing Machinery.
- LUO, T., WANG, Y., YUAN, Z., JIANG, Z., HUANG, W. & WANG, J. 2023 Large-eddy simulations of compressible Rayleigh–Taylor turbulence with miscible fluids using spatial gradient model. *Phys. Fluids* **35** (10), 105131.
- MAJUMDER, S., LIVESCU, D. & GIRIMAJI, S.S. 2024 Onset of kinetic effects on Rayleigh–Taylor instability: advective–diffusive asymmetry. *Phys. Fluids* **36** (12), 124113.
- MANDELBROT, B.B. 1982 *The Fractal Geometry of Nature*. Vol. 1. W. H. Freeman.
- MATHEW, G., MEZIĆ, I. & PETZOLD, L. 2005 A multiscale measure for mixing. *Physica D* **211** (1–2), 23–46.
- MATSUMOTO, T. 2009 Anomalous scaling of three-dimensional Rayleigh–Taylor turbulence. *Phys. Rev. E* **79** (5), 055301.
- MENEVEAU, C. 2011 Lagrangian dynamics and models of the velocity gradient tensor in turbulent flows. *Annu. Rev. Fluid Mech.* **43**, 219–245.
- MENEVEAU, C. & KATZ, J. 2000 *a, b* Scale-invariance and turbulence models for large-eddy simulation. *Annu. Rev. Fluid Mech.* **32** (1), 1–32.
- MEYER, C.R., MYDLARSKI, L. & DANAILA, L. 2018 Statistics of incremental averages of passive scalar fluctuations. *Phys. Rev. Fluids* **3** (9), 094603.
- NOMURA, K.K. & POST, G.K. 1998 The structure and dynamics of vorticity and rate of strain in incompressible homogeneous turbulence. *J. Fluid Mech.* **377**, 65–97.
- OUGHTON, S., MATTHAEUS, W.H., WAN, M. & PARASHAR, T. 2016 Variance anisotropy in compressible 3-D mhd. *J. Geophys. Res. Space Phys.* **121** (6), 5041–5054.
- PATTERSON, G.S. & ORSZAG, S.A. 1971 Spectral calculations of isotropic turbulence: efficient removal of aliasing interactions. *Phys. Fluids* **14** (11), 2538–2541.
- POINSOT, T. & VEYNANTE, D. 2005 *Theoretical and Numerical Combustion*. RT Edwards, Inc.
- POUJADE, O. 2006 Rayleigh–Taylor turbulence is nothing like Kolmogorov turbulence in the self-similar regime. *Phys. Rev. Lett.* **97** (18), 185002.
- QI, H., HE, Z., XU, A. & ZHANG, Y. 2024 The vortex structure and enstrophy of the mixing transition induced by Rayleigh–Taylor instability. *Phys. Fluids* **36** (11), 114107.
- RAYLEIGH 1883 Investigation of the character of the equilibrium of an incompressible heavy fluid of variable density. *Proc. Lond. Math. Soc.* **s1-14** (1), 170–177.
- RISTORCELLI, J.R. & CLARK, T.T. 2004 Rayleigh–Taylor turbulence: self-similar analysis and direct numerical simulations. *J. Fluid Mech.* **507**, 213–253.
- SADEK, M. & ALUIE, H. 2018 Extracting the spectrum of a flow by spatial filtering. *Phys. Rev. Fluids* **3** (12), 124610.
- SCHILLING, O. 2020 Progress on understanding Rayleigh–Taylor flow and mixing using synergy between simulation, modeling, and experiment. *J. Fluids Engng* **142** (12), 120802.
- SHEBALIN, J.V., MATTHAEUS, W.H. & MONTGOMERY, D. 1983 Anisotropy in MHD turbulence due to a mean magnetic field. *J. Plasma Phys.* **29** (3), 525–547.
- SMAGORINSKY, J. 1963 General circulation experiments with the primitive equations: I. The basic experiment. *Mon. Weather Rev.* **91** (3), 99–164.
- SOULARD, O. 2012 Implications of the Monin–Yaglom relation for Rayleigh–Taylor turbulence. *Phys. Rev. Lett.* **109** (25), 254501.

- SREENIVASAN, K.R. & MENEVEAU, C.J. 1986 The fractal facets of turbulence. *J. Fluid Mech.* **173**, 357–386.
- STORER, B.A., BUZZICOTTI, M., KHATRI, H., GRIFFIES, S.M. & ALUIE, H. 2022 Global energy spectrum of the general oceanic circulation. *Nat. Commun.* **13** (1), 5314.
- SYKES, J.P., GALLAGHER, T.P. & RANKIN, B.A. 2021 Effects of Rayleigh–Taylor instabilities on turbulent premixed flames in a curved rectangular duct. *Proc. Combust. Inst.* **38** (4), 6059–6066.
- TAYLOR, G. 1950 The instability of liquid surfaces when accelerated in a direction perpendicular to their planes. i. *Proc. R. Soc. Lond. A* **201** (1065), 192–196.
- TSENG, Y.-H. & FERZIGER, J.H. 2001 Effects of coastal geometry and the formation of cyclonic/anti-cyclonic eddies on turbulent mixing in upwelling simulation. *J. Turbul.* **2** (1), 014.
- VILLERMAUX, E. 2019 Mixing versus stirring. *Annu. Rev. Fluid Mech.* **51** (1), 245–273.
- WANG, C.-Y. & CHEVALIER, R.A. 2001 Instabilities and clumping in type Ia supernova remnants. *Astrophys. J.* **549** (2), 1119.
- WANG, M., YURIKUSA, T., IWANO, K., SAKAI, Y., ITO, Y., ZHOU, Y. & HATTORI, Y. 2023 Scale-by-scale analysis of interscale scalar transfer in grid turbulence with mean scalar gradient. *Phys. Fluids* **35** (4), 045153.
- WANG, Y., YUAN, Z., WANG, X. & WANG, J. 2022 Constant-coefficient spatial gradient models for the sub-grid scale closure in large-eddy simulation of turbulence. *Phys. Fluids* **34** (9), 095108.
- WARHAFT, Z. 2000 Passive scalars in turbulent flows. *Annu. Rev. Fluid Mech.* **32** (1), 203–240.
- WILSON, P.N. & ANDREWS, M.J. 2002 Spectral measurements of Rayleigh–Taylor mixing at small Atwood number. *Phys. Fluids* **14** (3), 938–945.
- XIAO, M.-J., QI, H. & ZHANG, Y.-S. 2025 Local transition indicator and modelling of turbulent mixing based on the mixing state. *J. Fluid Mech.* **1002**, A4.
- XIE, H., QI, H., XIAO, M., ZHANG, Y. & ZHAO, Y., 2025 An intermittency based Reynolds-averaged transition model for mixing flows induced by interfacial instabilities. *J. Fluid Mech.* **1002**, A31.
- XIN, J., YAN, R., WAN, Z.-H., SUN, D.-J., ZHENG, J., ZHANG, H., ALUIE, H. & BETTI, R. 2019 Two mode coupling of the ablative Rayleigh–Taylor instabilities. *Phys. Plasmas* **26** (3), 032703.
- XU, A., ZHANG, D. & GAN, Y. 2024 Advances in the kinetics of heat and mass transfer in near-continuous complex flows. *Front. Phys.* **19** (4), 42500.
- XU, A., ZHANG, G., YING, Y. & WANG, C. 2016 Complex fields in heterogeneous materials under shock: modeling, simulation and analysis. *Sci. China Phys. Mech. Astron.* **59**, 1–49.
- XU, A.-G., ZHANG, G.-C., GAN, Y.-B., CHEN, F. & YU, X.-J. 2012 Lattice Boltzmann modeling and simulation of compressible flows. *Front. Phys.* **7**, 582–600.
- YAGLOM, A.M. *et al.* 1949 On the local structure of a temperature field in a turbulent flow. *Dokl. Akad. Nauk SSSR* **69**, 743–746.
- YEUNG, P.K. & POPE, S.B. 1989 Lagrangian statistics from direct numerical simulations of isotropic turbulence. *J. Fluid Mech.* **207**, 531–586.
- YIN, H., SHANG, J.K., BLACKMAN, E.G., COLLINS, G.W. & ALUIE, H. 2023 Energy transfer and scale dynamics in 2D and 3D laser-driven jets. *Phys. Plasmas* **30** (9), 092309.
- YOUNGS, D.L. 1991 Three-dimensional numerical simulation of turbulent mixing by Rayleigh–Taylor instability. *Phys. Fluids A* **3** (5), 1312–1320.
- ZHANG, D., XU, A., SONG, J., GAN, Y., ZHANG, Y. & LI, Y. 2023 Specific-heat ratio effects on the interaction between shock wave and heavy-cylindrical bubble: based on discrete Boltzmann method. *Comput. Fluids* **265**, 106021.
- ZHANG, G., XU, A., ZHANG, D., LI, Y., LAI, H. & HU, X. 2021 Delineation of the flow and mixing induced by Rayleigh–Taylor instability through tracers. *Phys. Fluids* **33** (7), 076105.
- ZHANG, H., BETTI, R., GOPALASWAMY, V., YAN, R. & ALUIE, H. 2018a Nonlinear excitation of the ablative Rayleigh–Taylor instability for all wave numbers. *Phys. Rev. E* **97** (1), 011203.
- ZHANG, H., BETTI, R., YAN, R. & ALUIE, H. 2020 Nonlinear bubble competition of the multimode ablative Rayleigh–Taylor instability and applications to inertial confinement fusion. *Phys. Plasmas* **27** (12), 122701.
- ZHANG, H., BETTI, R., YAN, R., ZHAO, D., SHVARTS, D. & ALUIE, H. 2018b Self-similar multimode bubble-front evolution of the ablative Rayleigh–Taylor instability in two and three dimensions. *Phys. Rev. Lett.* **121** (18), 185002.
- ZHAO, D. & ALUIE, H. 2018 Inviscid criterion for decomposing scales. *Phys. Rev. Fluids* **3** (5), 054603.
- ZHAO, D. & ALUIE, H. 2023 Measuring scale-dependent shape anisotropy by coarse-graining: application to inhomogeneous Rayleigh–Taylor turbulence. *Phys. Rev. Fluids* **8** (11), 114601.
- ZHAO, D., BETTI, R. & ALUIE, H. 2022 Scale interactions and anisotropy in Rayleigh–Taylor turbulence. *J. Fluid Mech.* **930**, A29.
- ZHAO, D., XIAO, L., ALUIE, H., WEI, P. & LIN, C. 2023 Lagrangian investigation of the interface dynamics in single-mode Rayleigh–Taylor instability. *Phys. Fluids* **35** (10), 104103.

- ZHAO, Z., LIU, N.-S. & LU, X.-Y. 2020 Kinetic energy and enstrophy transfer in compressible Rayleigh–Taylor turbulence. *J. Fluid Mech.* **904**, A37.
- ZHOU, Y. 2001 A scaling analysis of turbulent flows driven by Rayleigh–Taylor and Richtmyer–Meshkov instabilities. *Phys. Fluids* **13** (2), 538–543.
- ZHOU, Y. 2017*a,b* Rayleigh–Taylor and Richtmyer–Meshkov instability induced flow, turbulence, and mixing. i. *Phys. Rep.* **720**, 1–136.
- ZHOU, Y. & CABOT, W.H. 2019 Time-dependent study of anisotropy in Rayleigh–Taylor instability induced turbulent flows with a variety of density ratios. *Phys. Fluids* **31** (8), 084106.
- ZHOU, Y., ROBEY, H.F. & BUCKINGHAM, A.C. 2003 Onset of turbulence in accelerated high-Reynolds-number flow. *Phys. Rev. E* **67** (5), 056305.
- ZHOU, Y., SADLER, J.D. & HURRICANE, O.A. 2025 Instabilities and mixing in inertial confinement fusion. *Annu. Rev. Fluid Mech.* **57**, 197–225.
- ZHOU, H., FENG, Q., HAO, P. & LI, L. 2021*a* Large eddy simulation of Rayleigh–Taylor mixing based on helicity model. *Intl J. Mod. Phys. C* **32** (04), 2150053.
- ZHOU, Y. *et al.* 2021*b,c*, Rayleigh–Taylor and Richtmyer–Meshkov instabilities: a journey through scales. *Physica D* **423**, 132838.
- ZINGALE, M., WOOSLEY, S.E., RENDLEMAN, C.A., DAY, M.S. & BELL, J.B. 2005 Three-dimensional numerical simulations of Rayleigh–Taylor unstable flames in type Ia supernovae. *Astrophys. J.* **632** (2), 1021.